Chapter 10
Electron Density as Carrier of Information

Abstract The information densities of electronic ground-state distributions are used as local probes of the chemical bonds in molecules. The entropy-deficiency and entropy-displacement relative to the promolecular electron density identify effects due to formation of the chemical bond. They reflect typical atom-promotion (polarization) and charge-transfer processes. The nonadditive information contributions to the density of molecular Fisher information (kinetic energy) of electrons are investigated in the MO and AO resolution levels. The former gives rise to the *Electron Localization Function*, while the latter is used to define the *Contra-gradience* criterion for locating the bonding regions in molecules. Illustrative applications to typical atomic/molecular systems are presented and discussed. They are seen to reflect quite adequately the system bonding pattern and the valence state of bonded atoms in the molecular environment, in accordance with intuitive chemical expectations.

10.1 Local Entropy-Deficiency (Surprisal) Analysis

As we have already remarked before, the electron densities $\{\rho_i^0\}$ of the separated atoms define the molecular (isoelectronic, $N = N^0$) prototype called the atomic "promolecule" (e.g., Hirshfeld 1977; Nalewajski 2006g), given by the sum of the atomic ground-state electron densities shifted to the actual locations of *Atoms-in-Molecules* (AIM). The resulting electron density $\rho^0 = \sum_i \rho_i^0$ of this collection of the "frozen" *free*-atom distributions defines the initial stage in the bond-formation process and determines a natural reference for extracting changes due to the chemical bonds in the familiar *density difference function* $\Delta\rho = \rho - \rho^0$. This deformation density has been widely used to probe the electronic structure of molecular systems. In this section we shall compare these plots with some local IT probes introduced in Chap. 8, to explore the molecular electron distributions $\rho(\boldsymbol{r})$ or their shape(probability) factors $p(\boldsymbol{r}) = \rho(\boldsymbol{r})/N$ generated using the KS LDA calculations.

R.F. Nalewajski, *Perspectives in Electronic Structure Theory*,
DOI 10.1007/978-3-642-20180-6_10,

Consider first the density $\Delta s(\boldsymbol{r})$ (in nats per unit volume) of the molecular KL entropy-deficiency (directed-divergence) reflecting the average information distance between the molecular and promolecular electron distributions:

$$\Delta S[\rho|\rho^0] = I^{\mathrm{KL}}[\rho|\rho^0] = \int \rho(\boldsymbol{r}) \ln[\rho(\boldsymbol{r})/\rho^0(\boldsymbol{r})]\, d\boldsymbol{r} = \int \rho(\boldsymbol{r}) I[w(\boldsymbol{r})]\, d\boldsymbol{r} \equiv \int \Delta s(\boldsymbol{r})\, d\boldsymbol{r}, \tag{10.1}$$

where $w(\boldsymbol{r}) = \rho(\boldsymbol{r})/\rho^0(\boldsymbol{r}) = p(\boldsymbol{r})/p^0(\boldsymbol{r})$ stands for the local *enhancement* factor of the density/probability distribution and $I[w(\boldsymbol{r})]$ denotes the associated *surprisal* function. The functional density $\Delta s(\boldsymbol{r})$ also represents the local (renormalized) missing information between the shape(probability) factors $p(\boldsymbol{r})$ and $p^0(\boldsymbol{r}) = \rho^0(\boldsymbol{r})/N^0$ of the two compared electron densities:

$$\Delta s(\boldsymbol{r}) \equiv \Delta s[\rho(\boldsymbol{r})|\rho^0(\boldsymbol{r})] = Np(\boldsymbol{r})\ \ln[p(\boldsymbol{r})/p^0(\boldsymbol{r})] \equiv N\Delta s[p(\boldsymbol{r})|p^0(\boldsymbol{r})]. \tag{10.2}$$

The KL-information density $\Delta s(\boldsymbol{r})$ thus measures the local value of the electron-density/probability-weighted surprisal of the electronic distribution relative to the promolecular reference. The related divergence measure of Kullback's (K) symmetrized missing information reads:

$$\begin{aligned} \Delta S[\rho, \rho^0] = I^{\mathrm{K}}[\rho, \rho^0] &= \int [\rho(\boldsymbol{r}) - \rho^0(\boldsymbol{r})] \ln[\rho(\boldsymbol{r})/\rho^0(\boldsymbol{r})] d\boldsymbol{r} \\ &\equiv \int \Delta\rho(\boldsymbol{r}) I[w(\boldsymbol{r})]\, d\boldsymbol{r} \equiv \int \Delta D(\boldsymbol{r})\, d\boldsymbol{r}. \end{aligned} \tag{10.3}$$

Therefore, its density $\Delta D(\boldsymbol{r})$ represents the local surprisal "weighted" by the density difference $\Delta\rho(\boldsymbol{r}) = \rho(\boldsymbol{r}) - \rho^0(\boldsymbol{r})$ or the probability difference $\Delta p(\boldsymbol{r}) = p(\boldsymbol{r}) - p^0(\boldsymbol{r}) = \Delta\rho(\boldsymbol{r})/N$:

$$\begin{aligned} \Delta D(\boldsymbol{r}) &\equiv \Delta s[\rho(\boldsymbol{r}), \rho^0(\boldsymbol{r})] = \Delta\rho(\boldsymbol{r}) I[w(\boldsymbol{r})] \\ &= N\Delta p(\boldsymbol{r}) I[w(\boldsymbol{r})] \equiv N\Delta s[p(\boldsymbol{r}), p^0(\boldsymbol{r})]. \end{aligned} \tag{10.4}$$

The molecular surprisal $I[w(\boldsymbol{r})]$ thus measures the density-per-electron of the local entropy-deficiency relative to the promolecular reference,

$$I[w(\boldsymbol{r})] = \Delta s(\boldsymbol{r})/\rho(\boldsymbol{r}), \tag{10.5}$$

or the density-per-electron–displacement of the molecular divergence,

$$I[w(\boldsymbol{r})] = \Delta D(\boldsymbol{r})/\Delta\rho(\boldsymbol{r}). \tag{10.6}$$

We further recall that the molecular electron density $\rho(\boldsymbol{r})$ is on average only slightly modified relative to the promolecular distribution $\rho^0(\boldsymbol{r})$, $\rho(\boldsymbol{r}) \approx \rho^0(\boldsymbol{r})$ or

$w(\boldsymbol{r}) \approx 1$. Indeed, the formation of chemical bonds involves only a minor reconstruction of the electronic structure, mainly in the *valence*-shells of the constituent atoms, so that $|\Delta\rho(\boldsymbol{r})| \equiv |\rho(\boldsymbol{r}) - \rho^0(\boldsymbol{r})| << \rho(\boldsymbol{r}) \approx \rho^0(\boldsymbol{r})$ and hence the ratio $\Delta\rho(\boldsymbol{r})/\rho(\boldsymbol{r}) \approx \Delta\rho(\boldsymbol{r})/\rho^0(\boldsymbol{r})$ is generally small in the energetically important regions of the large density values, near the atomic nuclei. As explicitly shown in the first column of Fig. 10.1, the largest values of the density difference $\Delta\rho(\boldsymbol{r})$ are observed mainly in the bond region, between the nuclei of chemically bonded atoms; the reconstruction of atomic lone pairs can also lead to an appreciable displacement in the molecular electron density in the outer regions of atomic densities.

By expanding the logarithm of the molecular surprisal $I[w(\boldsymbol{r})]$ around $w(\boldsymbol{r}) = 1$, to *first*-order in the relative displacement of the electron density, one obtains the following approximate relations between the local values of the molecular surprisal and the density-difference function:

$$\begin{aligned} I[w(\boldsymbol{r})] &= \ln[\rho(\boldsymbol{r})/\rho^0(\boldsymbol{r})] = \ln\{[\rho^0(\boldsymbol{r}) + \Delta\rho(\boldsymbol{r})]/\rho^0(\boldsymbol{r})\} \\ &\cong \Delta\rho(\boldsymbol{r})/\rho^0(\boldsymbol{r}) \approx \Delta\rho(\boldsymbol{r})/\rho(\boldsymbol{r}). \end{aligned} \tag{10.7}$$

This relation provides a semiquantitative information-theoretic interpretation of the relative density difference diagrams and links the local surprisal of IT to the density difference function of quantum chemistry (Nalewajski et al. 2002; Nalewajski and Świtka 2002). It also relates the integrands of the alternative information-distance functionals to the corresponding functions of displacements in the electron density:

$$\Delta s(\boldsymbol{r}) = \rho(\boldsymbol{r}) I[w(\boldsymbol{r})] \cong \Delta\rho(\boldsymbol{r}) w(\boldsymbol{r}) \approx \Delta\rho(\boldsymbol{r}), \tag{10.8}$$

$$\Delta D(\boldsymbol{r}) = \Delta\rho(\boldsymbol{r}) I[w(\boldsymbol{r})] \cong [\Delta\rho(\boldsymbol{r})]^2/\rho^0(\boldsymbol{r}) \geq 0. \tag{10.9}$$

The first of these relations qualitatively explains a remarkable similarity between the density difference and the KL information density plots observed in Fig. 10.1, where the contour maps of these quantities are reported for selected linear diatomics and triatomics.

The approximate equalities of (10.8) and (10.9) are numerically verified in Figs. 10.1 and 10.2, respectively. In the former, the contour diagram of the directed divergence density $\Delta s(\boldsymbol{r})$ is compared with the corresponding map of its *first*-order approximation, $\Delta\rho(\boldsymbol{r})w(\boldsymbol{r})$, and the density difference function $\Delta\rho(\boldsymbol{r})$ itself. A general similarity between these diagrams in each row of the figure confirms the semiquantitative character of the *first*-order expansions of the directed divergence densities. The corresponding numerical validation of (10.9) is shown in Fig. 10.2, where the contour maps of Kullback's divergence density $\Delta D(\boldsymbol{r})$ are compared with the corresponding diagrams of its *first*-order approximation $[\Delta\rho(\boldsymbol{r})]^2/\rho^0(\boldsymbol{r})$. Again, a remarkable similarity between the two diagrams in each row numerically validates this approximate relation thus also testifying to the overall smallness of the density adjustments due to the bond-formation processes in molecules.

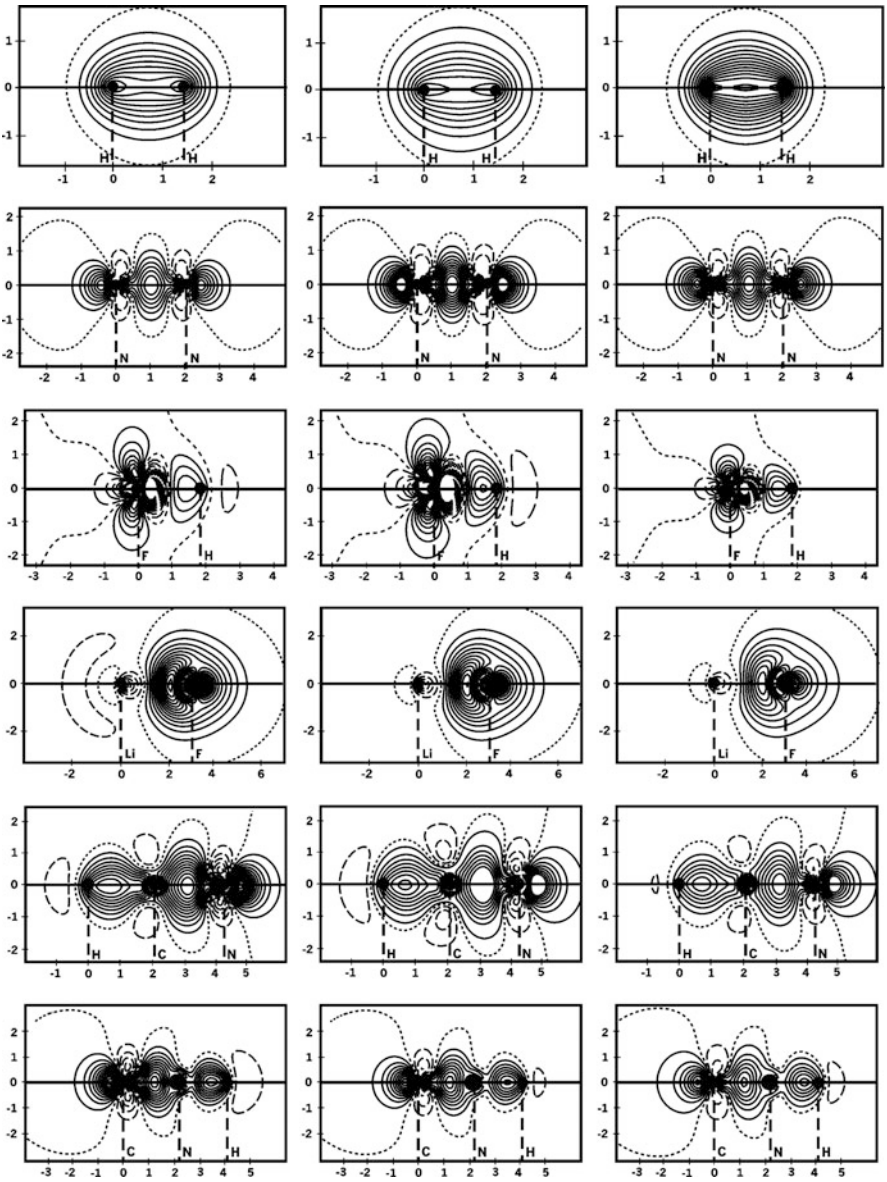

Fig. 10.1 Contour diagrams of the molecular density difference function, $\Delta\rho(\boldsymbol{r}) = \rho(\boldsymbol{r}) - \rho^0(\boldsymbol{r})$ (first column), the information-distance density, $\Delta s(\boldsymbol{r}) = \rho(\boldsymbol{r})I[w(\boldsymbol{r})]$ (second column) and its approximate, *first*-order expansion $\Delta s(\boldsymbol{r}) \cong \Delta\rho(\boldsymbol{r})w(\boldsymbol{r})$ (10.8) (third column), for selected diatomic and linear triatomic molecules: H_2, HF, LiF, HCN, and HNC. The solid, pointed, and broken lines denote the positive, zero, and negative values, respectively, of the equally spaced contours; the same convention is applied in Fig. 10.2

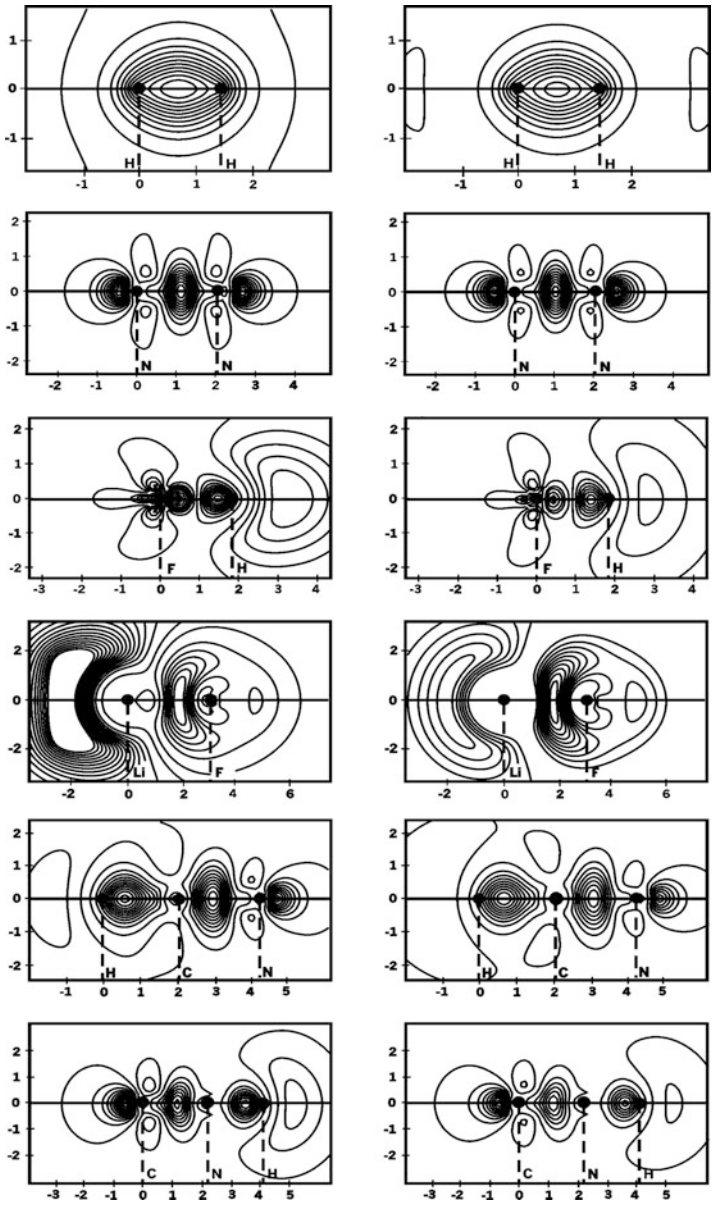

Fig. 10.2 A comparison between contour maps of the molecular divergence density, $\Delta D(\boldsymbol{r}) = \Delta\rho(\boldsymbol{r})I[w(\boldsymbol{r})]$ (first column) and its *first*-order term $[\Delta\rho(\boldsymbol{r})]^2/\rho^0(\boldsymbol{r})$ (second column), for molecules of Fig. 10.1, which validates the approximate relation (10.9)

In Fig. 10.1 the density difference function $\Delta\rho(\boldsymbol{r})$ for representative linear diatomic and triatomic molecules exhibits typical aspects of the equilibrium reconstructions of the *free* atoms during formation of the single and multiple

chemical bonds, which exhibit varying degree of the bond covalency (electron-sharing) and ionicity (electron-transfer) components. Let us first examine the contour maps for the two homonuclear diatomics. The single covalent bond in H_2 gives rise to a relative accumulation of electrons in the bond region, between the two nuclei, at the expense of the outer, nonbonding regions of space. The *triple*-bond pattern for N_2 is seen to be more complex, reflecting the density accumulations in the bonding region, due to both the σ and π bonds, and the accompanying increase in the density of the lone pairs on both nitrogen atoms, due to their expected *sp*-hybridization in the promoted valence state of each atom. One also observes a density decrease in the vicinity of the nuclei and an outflow of electrons from the $2p_\pi$ AO to their overlap area, a clear sign of these orbitals involvement in the formation of the double π bond.

Both heteronuclear diatomics, HF and LiF, represent partially ionic bonds between the two atoms exhibiting small and large differences in their electronegativity and chemical hardness descriptors, respectively. A pattern of the density displacement in HF reflects a weakly ionic (strongly covalent) bond, while in LiF the two AIM are seen to be connected by the strongly ionic (weakly covalent) bond. Indeed, in HF one detects a relatively high degree of a "common possession" of the valence electrons by the two atoms, which significantly contribute to the shared bond-charge located between them, and a comparatively weak H $\rightarrow$ F polarization. In LiF, a substantial Li $\rightarrow$ F CT can be detected so that an ion-pair picture indeed provides more adequate *zeroth*-order description of the chemical bond in this diatomic.

Finally, in the two triatomic molecules shown in Fig. 10.1, one identifies a strongly covalent pattern of the electron density displacements in the regions of the single N–H and C–H bonds. A typical buildup of the bond charge due to the multiple CN bonds in the two isomers HCN and HNC can be also observed. The increase in the lone-pair electron density on the terminal heavy atom, N in HCN and or C in HNC, can be also detected, thus again confirming the expected *sp*-hybridization of these bonded atoms in their promoted, valence states in the molecular environment.

A comparison between the corresponding panels of the first two columns in Fig. 10.1 shows that the two displacement maps so strongly resemble one another that they are hardly distinguishable. This confirms a close relation between the local density and entropy-deficiency relaxation patterns, thus attributing to the former the complementary IT interpretation of the latter. This strong resemblance between the two types of molecular diagrams also indicates that the local inflow of electrons increases the relative entropy, while the outflow of electrons gives rise to a diminished level of this relative-uncertainty content of the electron distribution in the molecule. The density displacement and the missing-information distribution can be thus viewed as equivalent probes of the system chemical bonds.

Similar diagnostic conclusions follow from the divergence density plots of Fig. 10.2, where all crucial bonding and nonbonding regions of space are now identified by the *positive* values of Kullback's symmetrized information-distance density. Therefore, all information-distance densities can indeed be regarded as

efficient tools for diagnosing the presence of chemical bonds and monitoring the effective valence states of the bonded atoms in molecules.

10.2 Displacements in Entropy Density

We shall now examine the molecular displacements in the average Shannon entropy, relative to the promolecular reference value,

$$\mathscr{H}[\rho] \equiv S[\rho] - S[\rho^0] = -\int \rho(\boldsymbol{r}) \ln \rho(\boldsymbol{r})\, d\boldsymbol{r} + \int \rho^0(\boldsymbol{r}) \ln \rho^0(\boldsymbol{r})\, d\boldsymbol{r} \equiv \int h_\rho(\boldsymbol{r})\, d\boldsymbol{r}, \tag{10.10}$$

and its density $h_\rho(\boldsymbol{r})$ as alternative candidates for the global/local probes of the electron distributions in molecules. The corresponding entropy shifts in terms of the unity-normalized probability distributions,

$$\mathscr{H}[p] \equiv S[p] - S[p^0] = -\int p(\boldsymbol{r}) \ln p(\boldsymbol{r})\, d\boldsymbol{r} + \int p^0(\boldsymbol{r}) \ln p^0(\boldsymbol{r})\, d\boldsymbol{r} \equiv \int h_p(\boldsymbol{r})\, d\boldsymbol{r}, \tag{10.11}$$

can also be used as alternative tools to explore the local relaxations in electron uncertainties, which accompany the chemical bond formation in molecules.

In Fig. 10.3, the contour maps of the entropy-displacement density $h_\rho(\boldsymbol{r})$ are compared with the corresponding density-difference diagrams $\Delta\rho(\boldsymbol{r})$ for the representative linear molecules of Fig. 10.1. To better visualize details of the two functions and to facilitate a qualitative comparison between their topographies, nonequidistant contour values have been selected. Therefore, only the profile of $h_\rho(\boldsymbol{r})$, shown in the third column of the figure, reflects the relative importance of each feature. When interpreting these plots one should realize that a negative (positive) value of $h_\rho(\boldsymbol{r})$ [or $h_p(\boldsymbol{r})$] signifies a decrease (increase) in the local electron *uncertainty* in the molecule, relative to the associated promolecular reference value.

Again, the $\Delta\rho$ and h_ρ diagrams for H_2 are seen to qualitatively resemble one another and the corresponding Δs map shown in Fig. 10.1. The main feature of the h_ρ diagram, an increase in the electron uncertainty in the bonding region between the two nuclei, is due to the inflow of electrons to this region. This manifests the bond-covalency phenomenon, which can be attributed to the electron-sharing effect and a delocalization of the bonding electrons, now effectively moving in the field of both nuclei. One detects in all these maps a similar nodal structure and finds that the nonbonding regions exhibit a decreased uncertainty, due to a transfer of the electron density from this area to the vicinity of the two nuclei and the region between them or as a result of the orbital hybridization (cylindrical polarization).

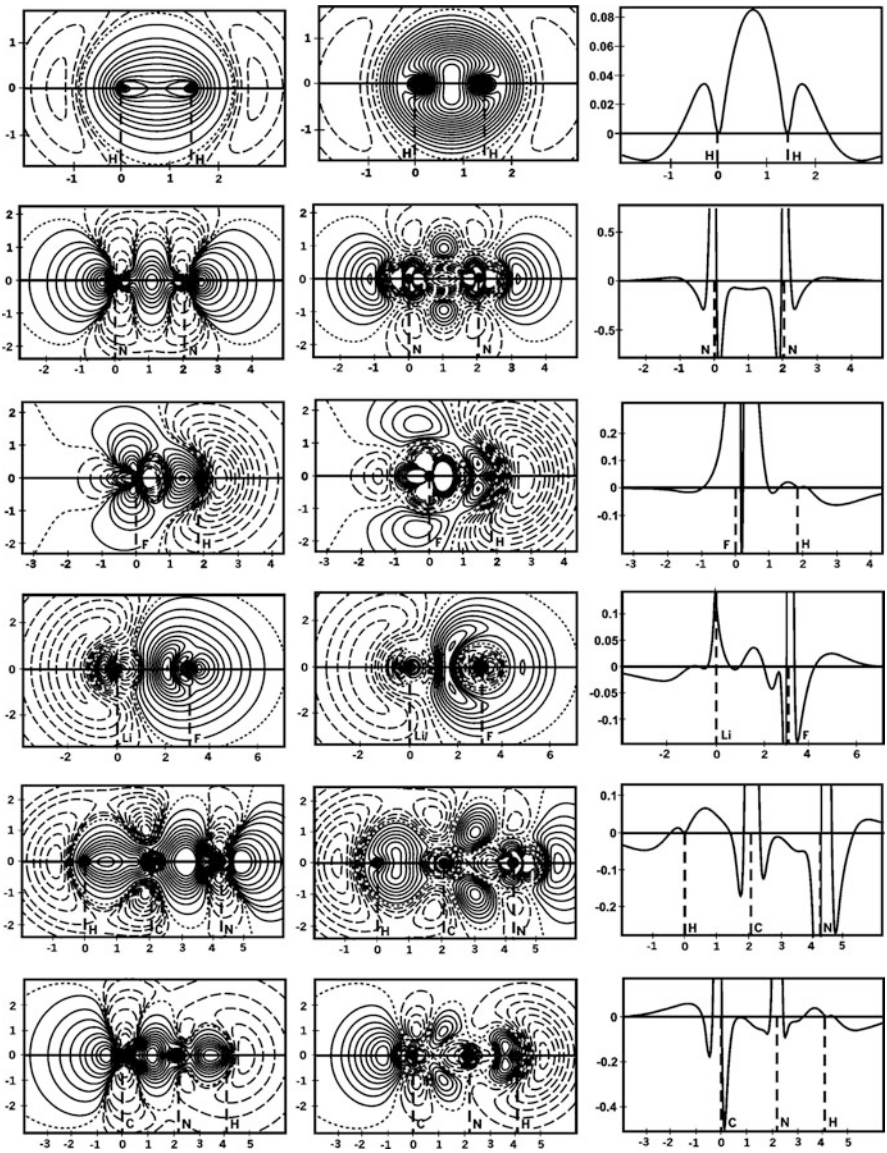

Fig. 10.3 A comparison between the (nonequidistant) contour diagrams of the density difference $\Delta\rho(\boldsymbol{r})$ (first column) and entropy-difference $h_\rho(\boldsymbol{r})$ (second column) functions for the linear molecules of Fig. 10.1. The corresponding profiles of $h_\rho(\boldsymbol{r})$ for the cuts along the bond axis are shown in the third column of the figure

Therefore, the molecular entropy difference function displays all typical features in the reconstruction of electron distributions in a molecule, relative to those of the corresponding free atoms. Its diagrams thus provide an alternative information tool

Table 10.1 Displacements of Shannon entropies (in bits) for molecules of Fig. 10.1

Molecule	$\mathcal{H}[\rho] \equiv S[\rho] - S[\rho^0]$	$S[\rho]$	$S[\rho^0]$
H_2	−0.84	6.61	7.45
N_2	−0.68	8.95	9.63
HF	−1.00	3.00	4.00
LiF	−3.16	5.12	8.28
HCN	−1.44	12.99	14.45
HNC	−1.39	13.06	14.45

for diagnosing the presence of chemical bonds through displacements in the entropy/information content of the molecular electron densities.

In fact, the comparison of Fig. 10.3 also demonstrates that, compared to the corresponding density difference diagrams, the entropy difference plots provide in many respects a more detailed account of the reorganization of the electronic structure relative to the free atoms in the promolecule, particularly in the *inner*-shell regions of heavy atoms.

In Table 10.1 we have listed the representative values of the molecular entropy difference (10.10) together with the associated Shannon entropies for the molecular and promolecular electron densities (Nalewajski and Broniatowska 2003a). These results show that in general the molecular distribution gives rise to a lower level of the information-entropy (less electron uncertainty) compared to the promolecule. This confirms an expected higher degree of compactness exhibited by electron distributions of the *bonded* atoms, which experience the presence of the remaining atoms, compared to their free (separated) analogs.

Thus, the degree of uncertainty contained in the electron distribution on average decreases when the constituent free atoms form the chemical bonds. Indeed, the dominating overall contraction of atomic electron distributions in the field of all nuclear attractors in the molecule should imply a higher degree of "order" (less uncertainty) in the molecular electron density in comparison to that present in the promolecular distribution. The largest magnitude of this relative decrease in the entropy content of the molecular electron density is observed for LiF, which exhibits the most ionic bond (largest amount of CT) among all molecules included in the table.

There is no apparent correlation in the table between the global entropy-displacement and the chemical bond multiplicity. For example, a triple covalent bond in N_2 generates less overall entropy loss than does a single bond in H_2. The reason for a low magnitude of the entropy-displacement in N_2 is the result of a mutual cancellation of the negative and positive contributions due to valence electrons. Indeed, the orbital hybridization and AO contraction should lower the entropy of the atomic electron distribution, since they increase charge inhomogeneity in the molecule, relative to the atomic promolecule. By the same criterion, the effective expansion of atomic densities due to the AIM promotion, as well as the electron delocalization *via* the system chemical bonds and the charge-transfer between AIM should have the opposite effect, of relatively increasing the uncertainty content of the electron distribution in the molecule. Notice that, should one assume a similar

entropy-displacement of about −0.7 bits for all triple bonds in a series of isoelectronic molecules N_2, HCN and CNH, one obtains a contribution due to a single C–H or N–H bond of about −0.7, a result close to that found for the H–H bond.

10.3 Illustrative Application to Propellanes

As an additional illustration we now present the combined density-difference, entropy-displacement, and the information-distance analysis of the central bond in small propellane systems (Nalewajski and Broniatowska 2003a). The main purpose of this study was to examine the effect on the central C′–C′ bond, between the (primed) "bridgehead" carbon atoms, of a successive increase in the size of the carbon bridges in the series of the [1.1.1], [2.1.1], [2.2.1], and [2.2.2] propellanes shown in Fig. 10.4. Figure 10.5 reports the contour maps of the molecular density difference function $\Delta\rho(\boldsymbol{r})$, the KL integrand $\Delta s(\boldsymbol{r})$, and the entropy-displacement density $h_\rho(\boldsymbol{r})$, for the planes of sections displayed in Fig. 10.4. The corresponding central-bond profiles of the density- and entropy-difference functions are shown in Fig. 10.6. The corresponding ground-state densities have been generated using the DFT-LDA calculations in the extended (DZVP) basis set.

The density difference plots show that in the small [1.1.1] and [2.1.1] propellanes there is on average a depletion of the electron density between the bridgehead carbon atoms, relative to the atomic promolecule, while the [2.2.1] and

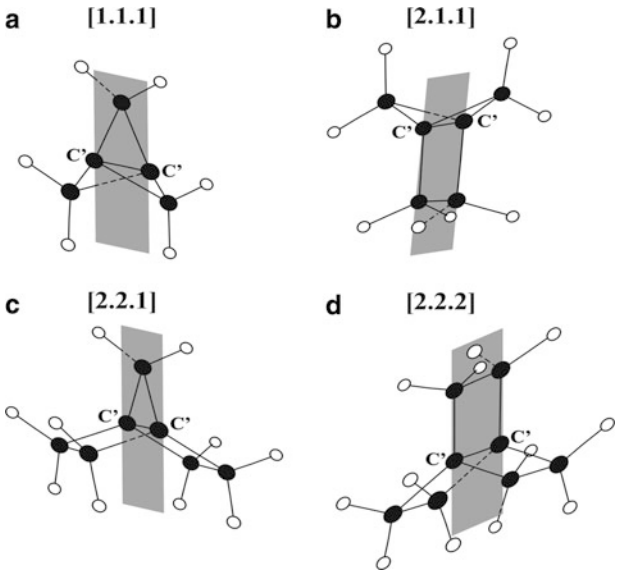

Fig. 10.4 The propellane structures and the planes of sections containing the bridge and bridgehead (C′) carbon atoms, identified by black circles

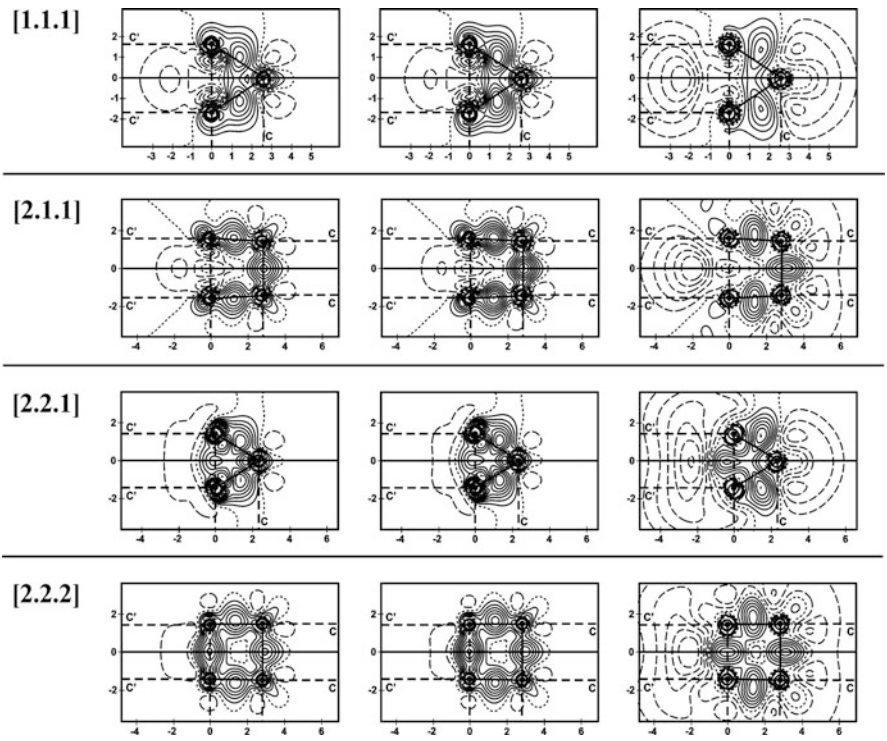

Fig. 10.5 A comparison between the equidistant contour maps of the density-difference function $\Delta\rho(\boldsymbol{r})$ (first column), the information-distance density $\Delta s(\boldsymbol{r})$ (second column), and the entropy-displacement density $h_\rho(\boldsymbol{r})$ (third column), for the four propellanes of Fig. 10.4

[2.2.2] systems exhibit a net density buildup in this region. A similar conclusion follows from the entropy-displacement and entropy-deficiency plots of these diagrams. The two entropic maps are again seen to be qualitatively similar to the corresponding density-difference plots. This resemblance is seen to be particularly strong between $\Delta\rho(\boldsymbol{r})$ and $\Delta s(\boldsymbol{r})$ diagrams shown in first two columns of Fig. 10.5.

In the generalized outlook on the bond-order concept (Nalewajski 2011a, b, c; Nalewajski and Gurdek 2010), emerging from extensions of both the Wiberg-type (Wiberg 1968; Gopinathan and Jug 1983; Mayer 1983, 1985; Jug and Gopinathan 1990) or the quadratic-difference approaches (Nalewajski et al. 1993, 1994a, 1996b, 1997; Nalewajski and Mrozek 1994, 1996; Mrozek et al. 1998; Nalewajski 2004b) to bond multiplicities in MO theory, and from the entropic bond-multiplicity concept in the *Orbital Communication Theory* (OCT) of the chemical bond (Nalewajski 2009e, f, g, 2010b, c, d, f; see also Chap. 12), one identifies the overall chemical bond multiplicity as a measure of the statistical "*dependence*" (nonadditivity) between orbitals on different atomic centers.

On one hand, this dependence between a given pair of AO on different atoms, the basis functions contributed to the bond system of the molecule, can be realized

directly (through space), by the constructive interference of these two orbitals, which increases the electron density between them. For the positive AO overlap it is then manifested by the positive value of the *off*-diagonal CBO (1-matrix) element coupling the two AO in the molecule. In OCT this through-space component, which signifies the absence of any AO intermediaries in the chemical interaction, originates from the *direct* probability/information scattering between the two AO under consideration.

On the other hand, such an interdependence between the two orbitals can also originate from *indirect* sources, through their chemical coupling to the remaining basis functions used to construct the system-occupied MO. Indeed, the orthonormality relations of the occupied MO, which determine the framework of chemical bonds in the molecule, introduce the implicit dependencies between orbitals, which generate the associated "through-bridge" bond-order contributions (Nalewajski 2011a,b,c,e,f; Nalewajski and Gurdek 2011a, b). In OCT this "cascade" bond component is effected through the *indirect* probability/information propagation between the specified pair of AO, through the specified subsets of the remaining basis functions (Nalewajski 2011e,f; Nalewajski and Gurdek 2011b). This component is thus realized through several AO-intermediates, which form an effective "bridge" for the probability/information scattering from one basis function to another.

Therefore, each pair of AO or AIM exhibits the partial through-*space* and through-*bridge* bond components. The bond-order of the former quickly decays with an increase in the interatomic separation. It is also small, when interacting orbitals are heavily engaged in forming chemical bonds with other atoms. The through-*bridge* bond-order, however, can still assume appreciable values, when the remaining atoms form an effective bridge of neighboring (bonded) atoms, which links the atomic pair in question. We shall discuss the basic concepts of this novel IT outlook on statistical origins of bond-orders in Chap. 12.

The numerical bond-orders reported in Fig. 10.6 originate from the *two*-electron difference approach (Nalewajski et al. 1993, 1994a, 1996a, b, 1997; Nalewajski and Mrozek 1994, 1996; Mrozek et al. 1998; Nalewajski 2004b), an extension of the original bond multiplicity index of Wiberg (1968) and its subsequent generalizations (Gopinathan and Jug 1983; Mayer 1983, 1985; Jug and Gopinathan 1990). Together with the corresponding density profiles shown in this figure they reveal a changing nature of the central bond in the four propellanes included in this analysis. The central "bonds" in the smallest systems, lacking the accumulation of the electron density or the entropy/entropy-deficiency density between the bridgehead atoms, are seen to be mostly of the *indirect* character, being realized through-bridges rather than directly through-space (Nalewajski 2011a,b,e,f). Clearly, the most important atomic intermediates for this indirect bond mechanism in propellanes are the *bridge* carbons, which strongly overlap (communicate) with the *bridgehead* carbons.

The missing through-space component in the smallest [1.1.1] system is due to nearly tetrahedral (sp^3) hybridization on the bridgehead carbons (see Sect. 12.10.6), optimum to form strong bonds with the bridging carbon atoms, with the three hybrids on each of these central atoms being used to form the chemical bonds with the bridge carbons and the fourth (nonbonding, *singly*-occupied) hybrid being

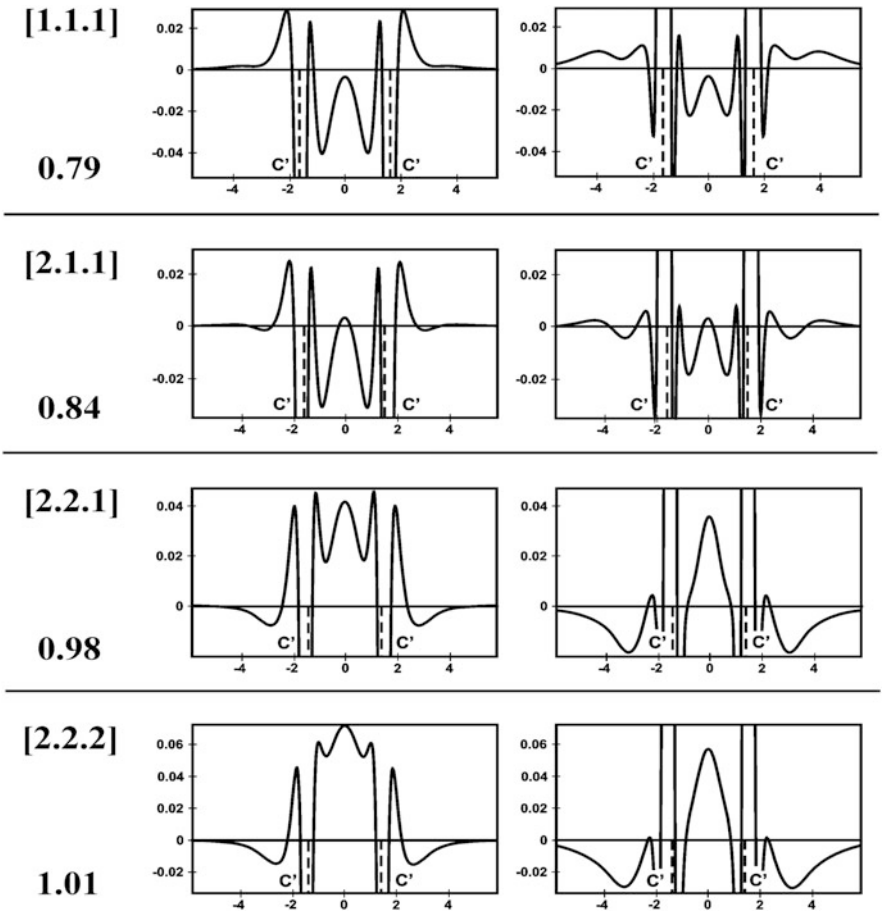

Fig. 10.6 The bridgehead bond profiles of the density difference function (*left panel*) and the molecular entropy-displacement (*right panel*) for the four propellanes shown in Fig. 10.4. For comparison the numerical values of the bond-multiplicities from the *two*-electron difference approach (Nalewajski et al. 1996b) are also reported

directed away from the central-bond region. In the largest [2.2.2] propellane these central carbons acquire a nearly trigonal (sp^2) hybridization, to form bonds with the bridge neighbors, with one $2p$ orbital, not used in this hybridization scheme, being now directed along the central-bond axis thus being capable of forming a strong through-space component of the overall multiplicity of the C′–C′ bond.

A gradual emergence of the direct, through-space component of the central bond, due to accumulation of the electron density and the entropy (entropy-deficiency) density between the bridgehead carbons, is observed when the bridges are enlarged in the two largest propellanes. Using the above *two*-electron difference approach one roughly estimates a full (single) central C′–C′ bond in the [2.2.1] and [2.2.2] propellanes, and approximately 0.8 (through-bridge) bond-order in the [1.1.1]

propellane. A more realistic orbital model of these interactions (Nalewajski 2011b) predicts for the largest [2.2.2] system the 0.62 of the direct Wiberg-type component and 0.14 of the indirect bond-order *via* the three double-carbon bridges, giving rise to the total measure of 0.76 bond multiplicity between the bridge-head carbons. The corresponding model estimate of the through-bridges chemical interaction in the smallest [1.1.1] propellane predict a weaker 0.40 bond-order. Therefore, the smaller system exhibits a higher through-bridge component, compensating for the lack of the direct central bond in this system, while the larger system generates almost twice as large overall bond multiplicity, mainly due to the direct component.

10.4 Nonadditive Information Measures

Each scheme $\rho = \sum_\alpha \rho_\alpha$ of exhaustively resolving the molecular ground-state electron density ρ into the corresponding pieces $\boldsymbol{\rho} = \{\rho_\alpha\}$ attributed to molecular fragments of interest, e.g., AIM, MO or AO, molecular fragments, etc., implies the associated division of the physical quantity $A \equiv A[\rho]$ into its subsystem additive and nonadditive components [Nalewajski 2003e, 2008e, 2010a, c, f; Nalewajski et al. 2010a, b; see also (7.372a)–(7.372c) in Sect. 7.8]:

$$A = A[\rho] \equiv A^{total}[\boldsymbol{\rho}] = A^{add.}[\boldsymbol{\rho}] + A^{nadd.}[\boldsymbol{\rho}]. \tag{10.12}$$

Indeed, by the Hohenberg–Kohn theorem A correspond to the unique functional of the ground-state density ρ, which defines the overall (*total*) multicomponent functional in the adopted subsystem resolution: $A^{total}[\boldsymbol{\rho}] \equiv A[\rho]$. This partition of the electron density also determines the associated *additive* contribution,

$$A^{add.}[\boldsymbol{\rho}] = \sum\nolimits_\alpha A[\rho_\alpha], \tag{10.13}$$

and hence also (indirectly) the *nonadditive* component:

$$A^{nadd.}[\boldsymbol{\rho}] = A^{total}[\boldsymbol{\rho}] - A^{add.}[\boldsymbol{\rho}] = A[\rho] - \sum\nolimits_\alpha A[\rho_\alpha]. \tag{10.14}$$

For example, this Gordon and Kim (1972) type division (see Sect. 7.8) of the kinetic energy functional defines its nonadditive contribution, which constitutes the basis of the DFT-embedding concept of Cortona (1991) and Wesołowski et al. (Wesołowski and Warshel 1993; Wesołowski et al. 1995; Wesołowski and Weber 1998; Nalewajski 2002f, 2003e; Wesołowski and Tran 2003; Wesołowski 2004a, b; Casida and Wesołowski 2004). It has also been demonstrated (Nalewajski et al. 2005) that the inverse of the nonadditive Fisher information in the MO resolution defines the IT-ELF concept, in spirit of the original ELF formulation by Becke and Edgecombe (1990), while the related quantity in the AO resolution of the SCF MO

theory offers the key *Contra-gradience* (CG) criterion for localizing the chemical bonds in molecular systems (Nalewajski 2008e, 2010f; Nalewajski et al. 2010a, b).

Such a division can also be used to partition the information quantities themselves (Nalewajski 2006g, 2010a, c). As an illustration consider the *local* partitioning of the molecular electron density into the AIM components, e.g., in the Hirshfeld ("stockholder") division, in which the molecular probability density at point $\boldsymbol{r}$ is divided into atomic contributions in accordance with the conditional probabilities (*share* factors) (Nalewajski and Parr 2000, 2001; Nalewajski 2002a, 2006g):

$$\begin{aligned} \boldsymbol{d}(\boldsymbol{r}) &= \{P(\mathrm{X}|\boldsymbol{r}) = p_{\mathrm{X}}(\boldsymbol{r})/p(\boldsymbol{r}) = \rho_{\mathrm{X}}(\boldsymbol{r})/\rho(\boldsymbol{r})\} \quad \text{or} \\ \boldsymbol{\rho}(\boldsymbol{r}) &= \{\rho_{\mathrm{X}}(\boldsymbol{r}) = Np_{\mathrm{X}}(\boldsymbol{r}) = \rho(\boldsymbol{r})P(\mathrm{X}|\boldsymbol{r})\}. \end{aligned} \tag{10.15a}$$

The promolecular reference similarly determines the initial conditional probabilities of the free atoms:

$$\begin{aligned} \boldsymbol{d}^0(\boldsymbol{r}) &= \{P^0(\mathrm{X}|\boldsymbol{r}) = p^0_{\mathrm{X}}(\boldsymbol{r})/p^0(\boldsymbol{r}) = \rho^0_{\mathrm{X}}(\boldsymbol{r})/\rho^0(\boldsymbol{r})\} \quad \text{or} \\ \boldsymbol{\rho}^0(\boldsymbol{r}) &= \{\rho^0_{\mathrm{X}}(\boldsymbol{r}) = Np^0_{\mathrm{X}}(\boldsymbol{r}) = \rho^0(\boldsymbol{r})P^0(\mathrm{X}|\boldsymbol{r})\}. \end{aligned} \tag{10.15b}$$

In this local partition scheme the overall distributions $\rho(\boldsymbol{r})$ [or $p(\boldsymbol{r}) = \rho(\boldsymbol{r})/N$] as well as $\rho^0(\boldsymbol{r})$ [or $p^0(\boldsymbol{r}) = \rho^0(\boldsymbol{r})/N$] and the associated promolecular conditional probabilities $\boldsymbol{d}^0(\boldsymbol{r})$ are assumed to be known from earlier molecular and atomic calculations, respectively. The "stockholder" division rule (Hirshfeld 1977) then assumes $\boldsymbol{d}(\boldsymbol{r}) = \boldsymbol{d}^0(\boldsymbol{r})$.

The overall KL missing-information density in this local partition of the electron density,

$$\Delta s[\rho;\boldsymbol{r}] = \rho(\boldsymbol{r})\log[\rho(\boldsymbol{r})/\rho^0(\boldsymbol{r})\}] = \rho(\boldsymbol{r})I(\boldsymbol{r}) \equiv \Delta s^{total}[\boldsymbol{\rho}(\boldsymbol{r})|\boldsymbol{\rho}^0(\boldsymbol{r})], \tag{10.16}$$

where $w(\boldsymbol{r})$ stands for the molecular enhancement factor relative to the promolecule and $I(\boldsymbol{r}) \equiv I[w(\boldsymbol{r})]$ denotes the associated surprisal, can be subsequently divided into its additive and nonadditive contributions in this atomic resolution:

$$\begin{aligned} \Delta s^{add.}[\boldsymbol{\rho}(\boldsymbol{r})|\boldsymbol{\rho}^0(\boldsymbol{r})] &= \sum\nolimits_{\mathrm{X}} \Delta s[\rho_{\mathrm{X}};\boldsymbol{r}], \\ \Delta s[\rho_{\mathrm{X}};\boldsymbol{r}] &= \rho_{\mathrm{X}}(\boldsymbol{r})\log[\rho_{\mathrm{X}}(\boldsymbol{r})/\rho^0_{\mathrm{X}}(\boldsymbol{r})] \equiv \rho_{\mathrm{X}}(\boldsymbol{r})\log w_{\mathrm{X}}(\boldsymbol{r}) \equiv \rho_{\mathrm{X}}(\boldsymbol{r})I_{\mathrm{X}}(\boldsymbol{r}); \end{aligned} \tag{10.17}$$

here $w_{\mathrm{X}}(\boldsymbol{r})$ again denotes the atomic *enhancement* factor and $I_{\mathrm{X}}(\boldsymbol{r}) \equiv I[w_{\mathrm{X}}(\boldsymbol{r})]$ stands for the associated local value of the atomic surprisal. Finally, the difference of the two entropy-deficiency densities determines the associated nonadditive contribution:

$$\Delta s^{nadd.}[\boldsymbol{\rho}(\boldsymbol{r})|\boldsymbol{\rho}^0(\boldsymbol{r})] = \Delta s^{total}[\boldsymbol{\rho}(\boldsymbol{r})|\boldsymbol{\rho}^0(\boldsymbol{r})] - \Delta s^{add.}[\boldsymbol{\rho}(\boldsymbol{r})|\boldsymbol{\rho}^0(\boldsymbol{r})]. \tag{10.18}$$

10.5 Electron Localization Function

Consider now the nonadditivities of the Fisher measure of information in the MO resolution, say, defined by the occupied KS MO from DFT calculations. In the spin-resolved approach one uses the energy functional of spin densities $\{\rho_\sigma(\boldsymbol{r})\}$, each defined by the spin-like electrons occupying the corresponding spin-subsets of MO $\boldsymbol{\psi} = \left\{ \boldsymbol{\psi}_\sigma = \{\psi_i^\sigma\} \right\}$,

$$\rho_\sigma(\boldsymbol{r}) = \sum_{i\in\sigma}^{occd.} \left|\psi_i^\sigma(\boldsymbol{r})\right|^2. \tag{10.19}$$

The (double) noninteracting kinetic energy density (a.u.),

$$2t_{s\sigma}[\boldsymbol{r},\rho_\sigma] \equiv \tau_\sigma[\boldsymbol{r};\rho_\sigma] = \sum_{i\in\sigma}^{occd.} \left|\nabla\psi_i^\sigma(\boldsymbol{r})\right|^2, \tag{10.20}$$

is then proportional to the distribution of the multicomponent (additive) Fisher information functional in the amplitude representation [see (8.7)],

$$I^{add.}[\boldsymbol{\psi}_\sigma] = 4\sum_{i\in\sigma}^{occd.} \int \left|\nabla\psi_i^\sigma(\boldsymbol{r})\right|^2 d\boldsymbol{r} \equiv \int f_\sigma^{add.}(\boldsymbol{r})\ d\boldsymbol{r}, \tag{10.21}$$

$$\tau_\sigma(\boldsymbol{r}) = \frac{1}{4} f_\sigma^{add.}(\boldsymbol{r}). \tag{10.22}$$

The leading term of the Taylor expansion of the spherically averaged HF (conditional) *pair*-probability of finding in distance s from the reference electron of spin σ at position $\boldsymbol{r}$ the other spin-like electron then reads (Becke and Edgecombe 1990; see also: Fuentalba et al. 2009):

$$P_c^{\sigma\sigma}(s|\boldsymbol{r}) = \frac{1}{3} D_\sigma(\boldsymbol{r}) s^2 + ...,$$
$$D_\sigma(\boldsymbol{r}) = \tau_\sigma(\boldsymbol{r}) - \frac{|\nabla\rho_\sigma(\boldsymbol{r})|^2}{4\rho_\sigma(\boldsymbol{r})} = -\frac{1}{4}[f_\sigma^{total}(\boldsymbol{r}) - f_\sigma^{add.}(\boldsymbol{r})] = -\frac{1}{4} f_\sigma^{nadd.}(\boldsymbol{r}) \ \geq 0. \tag{10.23}$$

Above, we have explicitly indicated that the function $D_\sigma(\boldsymbol{r})$, a key concept for the definition of ELF, is proportional to the negative nonadditive component of the Fisher information in the spin-resolved MO resolution.

The appropriately calibrated square of its inverse, which determines the original ELF, has been successfully used as a probe of the electron localization patterns in atoms (Fig. 10.7) and molecules (Nalewajski et al. 2005). Indeed, the magnitude of

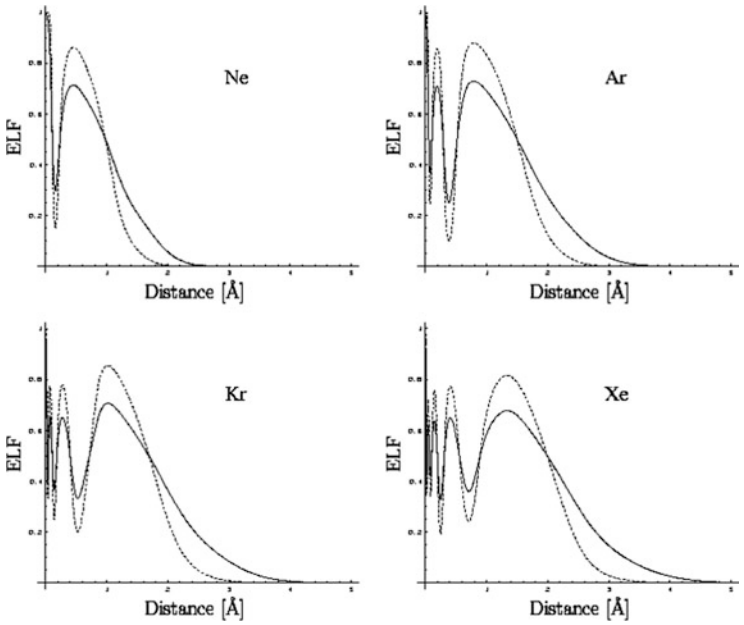

Fig. 10.7 Plots of ELF (*dashed line*) and IT-ELF (*solid line*) for Ne, Ar, Kr, and Xe

the (negative) nonadditive information component increases with the electron *delocalization*; therefore, its inverse reflects the complementary aspect of the electron *localization*. When supplemented with elements of the distribution topological analysis, the ELF concept provides a powerful tool for approaching many problems in structural chemistry (Silvi and Savin 1994; Savin et al. 1997).

A somewhat improved behavior at long distances is observed in the DFT-tailored simple inverse of this function, known as IT-ELF (Nalewajski et al. 2005). In Fig. 10.7, representative graphs of both functions are presented for Ne, Ar, Kr, and Xe. A qualitative behavior of the two curves is seen to be very similar, emphasizing the shell structure of these noble gas atoms. One also observes that ELF exhibits a faster decay at large distances from the nucleus and thus gives rise to smaller spatial extension of the valence basins compared to those in IT-ELF.

In Fig. 10.8, we have compared the perspective views of these functions for N_2, NH_3, PH_3, and B_2H_6. These ELF plots convincingly validate the use of this local probe as an indicator of the localization of the valence electrons in the bonding and nonbonding (lone-pair) regions of these illustrative molecular systems. Indeed, in the homonuclear diatomic N_2 one detects in both plots the typical accumulation of electrons between the nuclei, due to the formation of the triple covalent bond, and the accompanying increase in the localization of the lone-pair electrons in the nonbonding regions of both atoms, a clear manifestation of the accompanying *sp*-hybridization. The three localized N–H bonds are also clearly visualized in

both NH_3 panels of the figure and a similar ELF features are detected in its PH_3 part. The final B_2H_6 plots are also seen to successfully locate the bonding electrons of the four terminal B–H bonds.

The final application, shown in Fig. 10.9, again investigates the direct central and bridge bonds between the carbon atoms in the smallest [1.1.1] and largest [2.2.2] propellanes of Fig. 10.4. In these contour maps the absence (presence) of the through-space component of the central bond, between the bridgehead carbon atoms, is clearly seen in the upper (lower) panel for both versions of ELF, while the structure of the C–C bonds in the bridges is also transparently revealed. An interesting feature of the bridge bonds in the upper diagrams, also seen in Fig. 10.5, is a slight displacement of the bonding electrons away from the line connecting the bridge and bridgehead carbons, due to the near sp^3-hybridization on the bridge-carbon, which is required to additionally accommodate the two hydrogen atoms (Nalewajski 2010l).

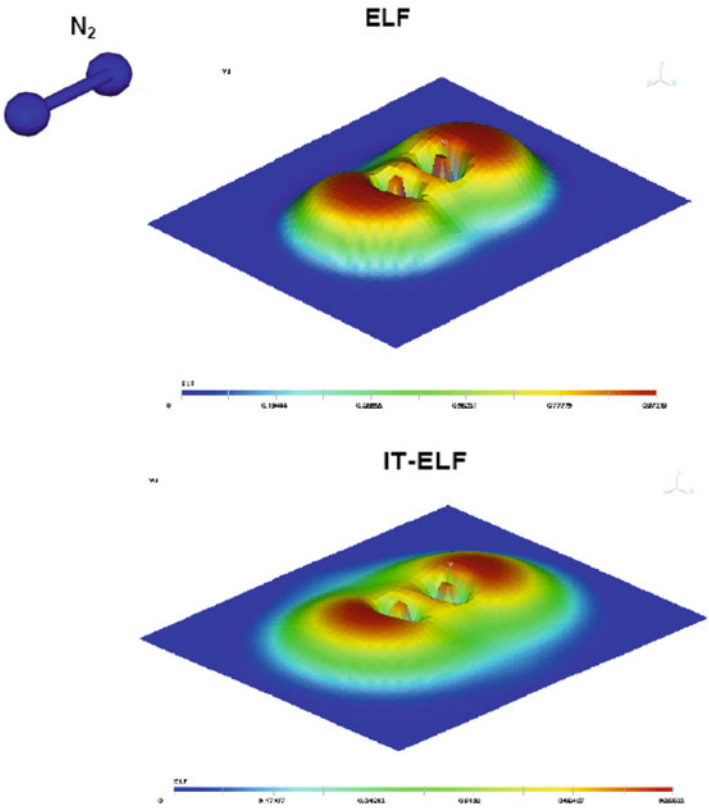

Fig. 10.8 (continued)

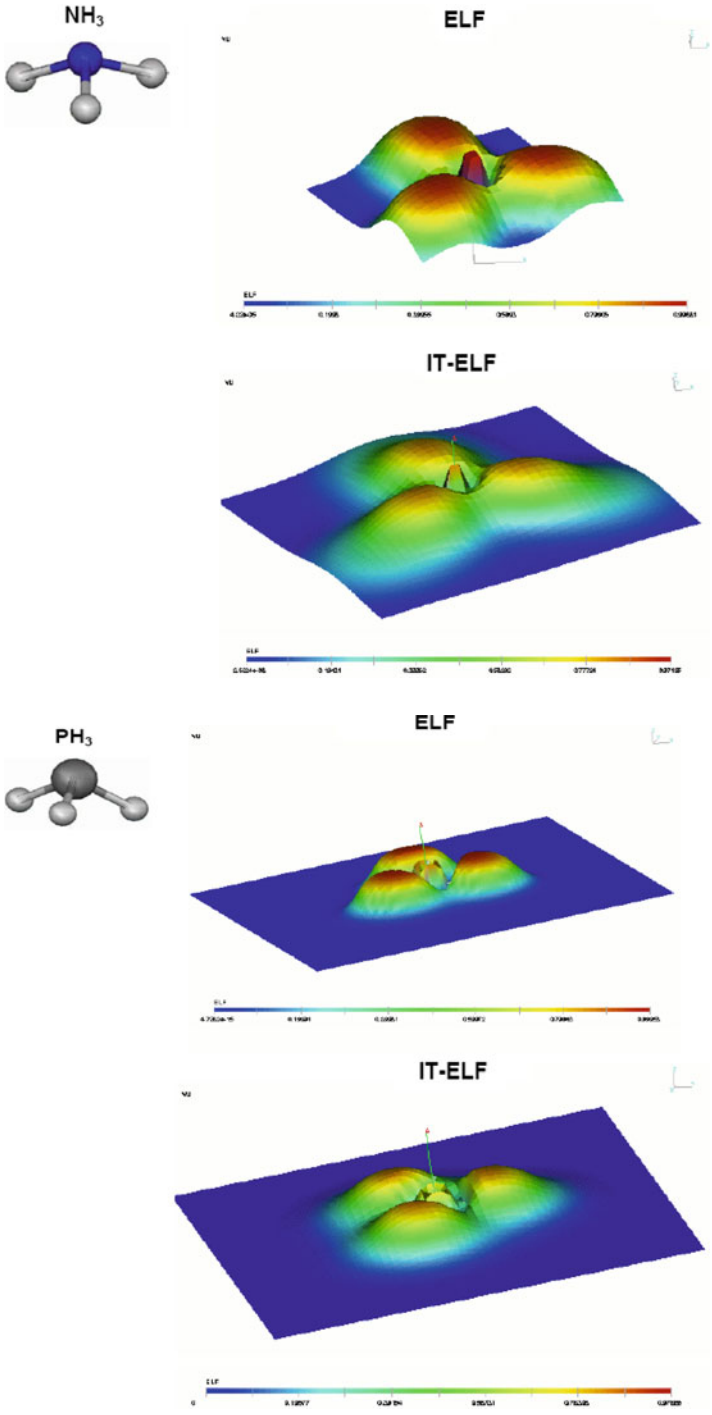

Fig. 10.8 (continued)

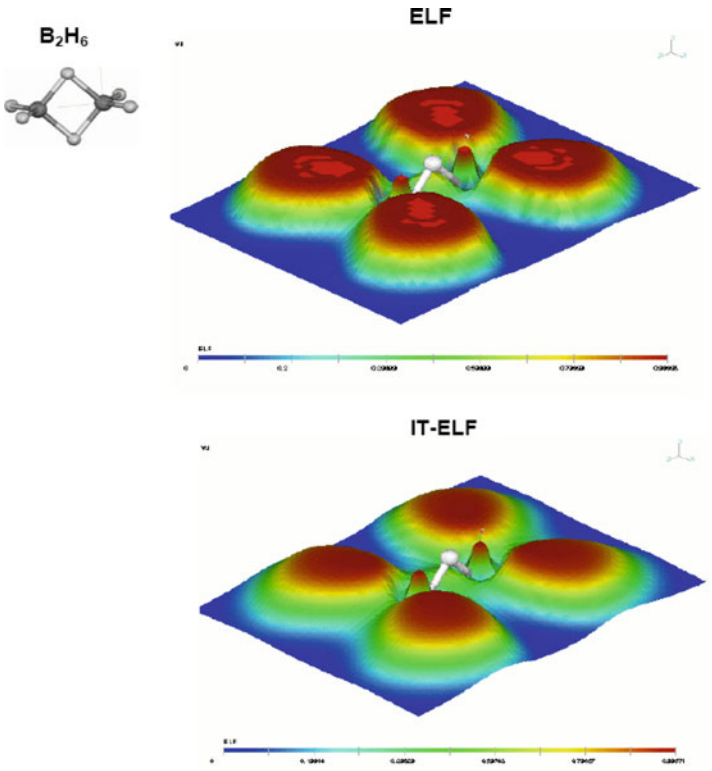

Fig. 10.8 Comparison between perspective views of the ELF and IT-ELF surfaces for N_2, NH_3, PH_3, and B_2H_6, on the corresponding planes of section: along the bond axis (N_2), in the plane determined by three hydrogen atoms (NH_3 and PH_3), and in the plane passing through both terminal BH_2 groups (B_2H_6), respectively

10.6 Contra-gradience Criterion for Locating Bonding Regions in Molecules

Consider next the familiar problem of combining the two (Löwdin-orthogonalized) AO (OAO), $A(\boldsymbol{r})$ and $B(\boldsymbol{r})$, say, two $1s$ orbitals centered on nuclei A and B, respectively, which contribute a single electron each, $N = 2$, to form the chemical bond A—B. The two basis functions $\boldsymbol{\chi} = (A, B)$ then form the bonding (φ_b) and antibonding (φ_a) MO combinations, $\boldsymbol{\varphi} = (\varphi_b, \varphi_a) = \boldsymbol{\chi}\mathbf{C}$:

$$\varphi_b = \sqrt{P}A + \sqrt{Q}B \equiv \sum\nolimits_{k=A,B} \chi_k C_{k,b}, \quad \varphi_a = -\sqrt{Q}A + \sqrt{P}B \equiv \sum\nolimits_{k=A,B} \chi_k C_{k,a}, \quad P + Q = 1, \tag{10.24}$$

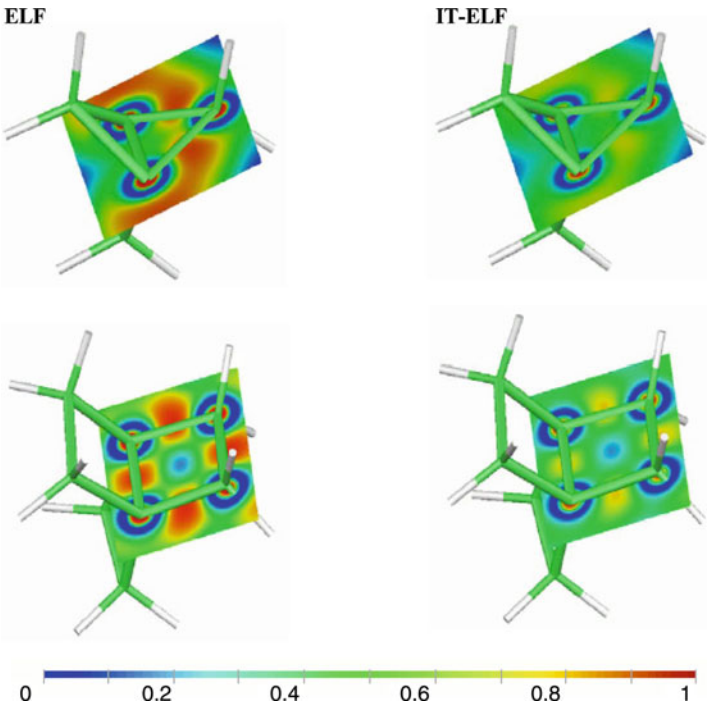

Fig. 10.9 Plots of the ELF(first column) and IT-ELF (second column) for the [1.1.1] (top row) and [2.2.2] (bottom row) propellanes of Fig. 10.4, on the indicated planes of section. The color scale for the ELF values is given in the bottom of the figure

where the square matrix $\mathbf{C} = [\boldsymbol{C}_b, \boldsymbol{C}_a]$ groups the LCAO MO expansion coefficients expressed in terms of the complementary probabilities: P and $Q = 1-P$. The former marks the conditional probabilities $P(A|\varphi_b) = |C_{A,b}|^2 = P(B|\varphi_a) = |C_{B,a}|^2 \equiv P$, and the latter measures the remaining elements of the conditional-probability matrix, of observing AO in MO: $P(B|\varphi_b) = |C_{B,b}|^2 = P(A|\varphi_a) = |C_{A,a}|^2 = Q$.

We now examine the (bonding) ground-state, $\Psi_0 = \left[\varphi_b^2\right]$, the (nonbonding) *singly* excited configuration $\Psi_1 = \left[\varphi_b^1\varphi_a^1\right]$, and the (antibonding) *doubly* excited state $\Psi_2 = \left[\varphi_a^2\right]$. Consider the *charge-and-bond-order* (CBO), density matrix of the SCF LCAO MO theory for each of these model configurations,

$$\begin{aligned}\boldsymbol{\gamma}_i &= \mathbf{C}\,\mathbf{n}(\Psi_i)\mathbf{C}^{\mathrm{T}} = \left\langle \boldsymbol{\chi} \,\middle|\, \boldsymbol{\psi}^{occd.}(\Psi_i)\right\rangle \mathbf{n}(\Psi_i)\left\langle \boldsymbol{\psi}^{occd.}(\Psi_i) \,\middle|\, \boldsymbol{\chi}\right\rangle \\ &= N\left\langle \boldsymbol{\chi} \,\middle|\, \boldsymbol{\psi}^{occd.}(\Psi_i)\right\rangle \mathbf{p}(\Psi_i)\left\langle \boldsymbol{\psi}^{occd.}(\Psi_i) \,\middle|\, \boldsymbol{\chi}\right\rangle = N\langle \boldsymbol{\chi}|\hat{\mathrm{d}}(\Psi_i)|\boldsymbol{\chi}\rangle, \quad i = 0, 1, 2,\end{aligned} \tag{10.25}$$

with the diagonal matrix of the MO electron occupations $\{n_s(\Psi_i)\}$, $\mathbf{n}(\Psi_i) = \{n_s(\Psi_i)\delta_{s,s'}\} = N\mathbf{p}(\Psi_i) = \{Np_s(\Psi_i)\delta_{s,s'}\}$, reflecting the MO probabilities $\{p_s(\Psi_i) = n_s(\Psi_i)/N\}$ in the electron configuration under consideration. As shown in the

preceding equation, this matrix constitutes the OAO representation of the density operator $\hat{d}(\Psi_i)$ determined by the appropriate statistical mixture of the subspace of the *singly* occupied spin-MO in the given electron configuration Ψ_i, $\boldsymbol{\psi}^{occd.}(\Psi_i)$. The three CBO matrices of the preceding equation read:

$$\boldsymbol{\gamma}_0 = 2\begin{bmatrix} P & \sqrt{PQ} \\ \sqrt{PQ} & Q \end{bmatrix}, \quad \boldsymbol{\gamma}_1 = \begin{bmatrix} 1 & 0 \\ 0 & 1 \end{bmatrix}, \quad \boldsymbol{\gamma}_2 = 2\begin{bmatrix} Q & -\sqrt{PQ} \\ -\sqrt{PQ} & P \end{bmatrix}. \tag{10.26}$$

They are seen to reflect the configuration bonding status. Indeed, the (bonding) ground state exhibits the positive *off*-diagonal bond-order, $\gamma_{A,B} = 2(PQ)^{1/2}$, which vanishes in the nonbonding configuration Ψ_1, $\gamma_{A,B} = 0$, while its negative value in Ψ_2, $\gamma_{A,B} = -2(PQ)^{1/2}$, correctly reflects the configuration antibonding character.

In this (real) 2-OAO model the AO-partition of the Fisher information densities of the bonding and antibonding MO gives the following total MO information densities:

$$\begin{aligned} f_b = 4(\nabla\varphi_b)^2 \equiv f_{\boldsymbol{\chi}}^{total}[\varphi_b] &= 4[P(\nabla A)^2 + Q(\nabla B)^2] + 8\sqrt{PQ}\nabla A \cdot \nabla B \\ &\equiv f_{\boldsymbol{\chi}}^{add.}[\varphi_b] + f_{\boldsymbol{\chi}}^{nadd.}[\varphi_b], \end{aligned} \tag{10.27}$$

$$\begin{aligned} f_a = 4(\nabla\varphi_a)^2 \equiv f_{\boldsymbol{\chi}}^{total}[\varphi_a] &= 4[Q(\nabla A)^2 + P(\nabla B)^2] - 8\sqrt{PQ}\nabla A \cdot \nabla B \\ &\equiv f_{\boldsymbol{\chi}}^{add.}[\varphi_a] + f_{\boldsymbol{\chi}}^{nadd.}[\varphi_a]. \end{aligned} \tag{10.28}$$

Along the bond-axis, in the AO-overlap region between the two atoms, which is decisive for the (direct) bonding or antibonding character of MO, the CG density defined by the product of gradients of the two interacting basis functions is negative: $i^{c-g} = \nabla A \cdot \nabla B < 0$ (see Fig. 10.10). Therefore, for these crucial locations

$$\begin{aligned} f_{\boldsymbol{\chi}}^{nadd.}[\varphi_b] &= 8\sqrt{PQ}\,\nabla A \cdot \nabla B \equiv 8\sqrt{PQ}\; i^{c-g} < 0, \\ f_{\boldsymbol{\chi}}^{nadd.}[\varphi_a] &= -8\sqrt{PQ}\,\nabla A \cdot \nabla B = -8\sqrt{PQ}\; i^{c-g} > 0. \end{aligned} \tag{10.29}$$

One similarly defines the average densities of the nonadditive and additive Fisher information contributions per electron for the configuration in question:

$$\begin{aligned} f_{\boldsymbol{\chi}}^{nadd.}[\Psi_i] &= \sum\nolimits_s [n_s(\Psi_i)/N] f_{\boldsymbol{\chi}}^{nadd.}[\varphi_s] \equiv \sum\nolimits_s p_s(\Psi_i) f_{\boldsymbol{\chi}}^{nadd.}[\varphi_s], \\ f_{\boldsymbol{\chi}}^{add.}[\Psi_i] &= \sum\nolimits_s p_s(\Psi_i) f_{\boldsymbol{\chi}}^{add.}[\varphi_s]. \end{aligned} \tag{10.30}$$

In particular, for the three model electron configurations one finds:

$$f_{\boldsymbol{\chi}}^{nadd.}[\Psi_0] = 8\sqrt{PQ}\, i^{c-g}, \quad f_{\boldsymbol{\chi}}^{nadd.}[\Psi_1] = 0, \quad f_{\boldsymbol{\chi}}^{nadd.}[\Psi_2] = -8\sqrt{PQ}\, i^{c-g}. \tag{10.31}$$

Therefore, the AO-phase-dependent, nonadditive contribution to the MO Fisher information density, proportional to the CG integral

$$I^{c-g} = \int i^{c-g}(\boldsymbol{r})\, d\boldsymbol{r} = \int \nabla A(\boldsymbol{r}) \cdot \nabla B(\boldsymbol{r})\; d\boldsymbol{r} = -\int A(\boldsymbol{r})\, \Delta B(\boldsymbol{r})\; d\boldsymbol{r}$$
$$= \frac{2m_e}{\hbar^2} \langle A|\, \hat{\mathrm{T}}|B\rangle \equiv \frac{2m_e}{\hbar^2} T_{A,B}, \tag{10.32}$$

reflects the bonding and antibonding characters of both MO as well as the bonding, nonbonding, and antibonding nature of the model configurations Ψ_0, Ψ_1, and Ψ_2, respectively. It thus provides an attractive concept for both locating and indexing the chemical bonds in molecules (Nalewajski 2010a, g; Nalewajski et al. 2010a, b).

As also indicated in the preceding equation, the CG integral measures the coupling (*off*-diagonal) element $T_{A,B}$ of the electronic kinetic energy operator $\hat{\mathrm{T}}$ between the two basis functions. Such integrals are routinely calculated in typical quantum-chemical packages for determining the electronic structure of molecular systems. This observation also emphasizes the crucial role of the kinetic energy terms in the IT interpretations of the entropic origins of the chemical bonding, using the Fisher measure of information.

A reference to Fig. 10.10 indicates that the $i^{c-g}(\boldsymbol{r}) = 0$ contour is defined by the equation $\boldsymbol{r}_{\mathrm{A}} \cdot \boldsymbol{r}_{\mathrm{B}} = 0$. It separates the region of positive contributions $i^{c-g}(\boldsymbol{r}) > 0$, outside this contour, from the region of negative CG density, $i^{c-g}(\boldsymbol{r}) < 0$, inside the contour. Consider, e.g., its section in *xz*-plane, for $y = 0$. For the Cartesian reference frame located at the bond midpoint and the two nuclei in positions $\boldsymbol{R}_{\mathrm{A}} = (0, 0, -½R)$ and $\boldsymbol{R}_{\mathrm{B}} = (0, 0, ½R)$, where the internuclear separation $R_{\mathrm{AB}} = R$, the electron-position vectors $\{\boldsymbol{r}_{\mathrm{X}} = \boldsymbol{r} - R_{\mathrm{X}}\}$ in this plane of section are: $\boldsymbol{r}_{\mathrm{A}} = (x, 0, z + ½R)$ and $\boldsymbol{r}_{\mathrm{B}} = (x, 0, z - ½R)$. The equation determining the $i^{c-g}(\boldsymbol{r}) = 0$ contour

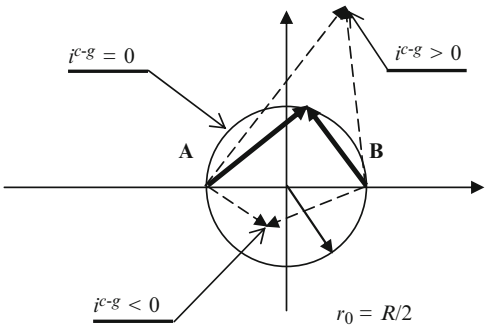

Fig. 10.10 The circular contour of the vanishing CG integrand for two 1*s* orbitals on atoms A and B, $i^{c-g}(\boldsymbol{r}) = 0$, passing through both nuclei, which separates the *bonding region* (inside the circle), where $i^{c-g}(\boldsymbol{r}) < 0$, from the region of positive contributions $i^{c-g}(\boldsymbol{r}) > 0$ (outside the circle). At each location $\boldsymbol{r}$ the sign of $i^{c-g}(\boldsymbol{r})$ is determined by the scalar product of the electron-position vectors $\boldsymbol{r}_\alpha = \boldsymbol{r} - \boldsymbol{R}_\alpha$, α = A, B, which are mutually perpendicular on the zero contour passing through both nuclei

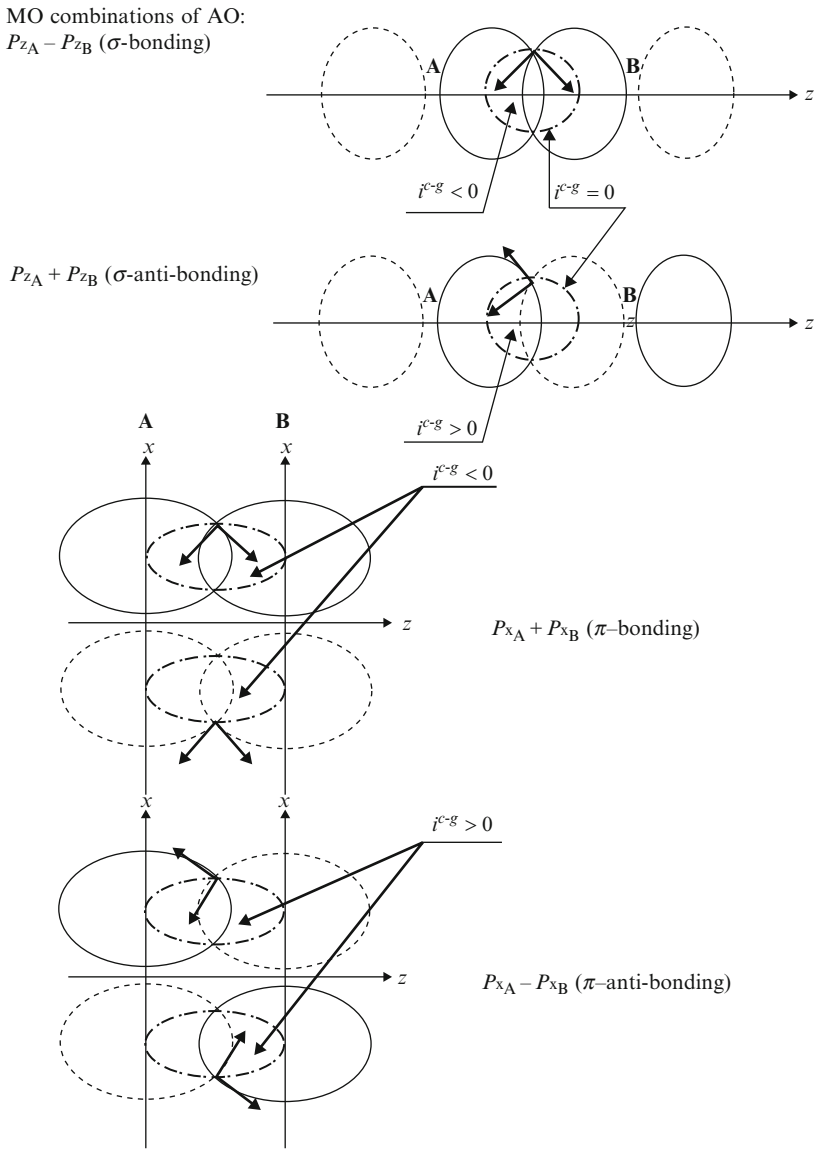

Fig. 10.11 Schematic representation of the bonding [$i^{c-g}(\boldsymbol{r}) < 0$] and antibonding [$i^{c-g}(\boldsymbol{r}) > 0$] regions of the strong AO overlap in the chemical interaction between the valence orbitals p_σ and p_π on atoms A and B, enclosed by the vanishing CG contours, $i^{c-g}(\boldsymbol{r}) = 0$, represented by the pointed–broken line. The AO gradients, each in the direction perpendicular to the orbital contour, remain mutually perpendicular on the $i^{c-g}(\boldsymbol{r}) = 0$ surface (see also Fig. 10.10). It again follows from these qualitative diagrams that the negative density of the nonadditive Fisher information accompanies the electron delocalization via the *constructive*-combination of AO in the bonding MO, while the positive density of this information contribution is associated with an effective electron localization, due to the *destructive*-combination of AO in the antibonding MO.

then reads: $x^2 + z^2 = (\frac{1}{2}R)^2 \equiv r_0^2$. It thus determines the circle shown in the figure, centered at the bond midpoint and passing through both nuclei.

As also argued in the qualitative diagram of Fig. 10.11, the negative CG density is essential for any bonding interaction between basis functions, e.g., the two p-type orbitals. Therefore, it is vital for the direct *bonding* interaction between a given pair of basis functions that the gradient of one orbital exhibits a nonvanishing, *negative* component along the direction of the gradient of the other orbital, which justifies the name of the CG criterion itself.

10.7 Illustrative Applications of CG Probe

In the ground-state of N-electron system and the OAO basis set $\boldsymbol{\chi} = (\chi_1, \chi_2, \ldots, \chi_m)$ the nonadditive Fisher information density in the AO resolution for the electron configuration defined by N lowest (*singly*-occupied) molecular *spin*-orbitals $\boldsymbol{\psi} = \{\psi_k\}$, with the spatial MO parts $\boldsymbol{\varphi} = \boldsymbol{\chi}\mathbf{C} = \{\varphi_k,\ k = 1, 2, ..., N\}$, e.g., those from the SCF MO or KS calculations, reads:

$$I^{nadd.}[\boldsymbol{\chi}] = 4\sum_{k=1}^{m}\sum_{l=1}^{m}(1-\delta_{k,l})\int \gamma_{k,l}\nabla\chi_l^*(\boldsymbol{r})\cdot\nabla\chi_k(\boldsymbol{r})\,d\boldsymbol{r} \equiv 2\int f^{nadd.}(\boldsymbol{r})\,d\boldsymbol{r}$$
$$= 8T^{nadd.}[\boldsymbol{\chi}], \tag{10.33}$$

where the CBO (density) matrix now provides the AO representation of the projection operator onto the occupied subspace of SO, $\hat{\mathrm{d}}(\Psi_0) = \hat{\mathrm{P}}_{\boldsymbol{\psi}} = |\boldsymbol{\psi}\rangle\langle\boldsymbol{\psi}|$,

$$\boldsymbol{\gamma} = \langle\boldsymbol{\chi}|\left(\sum_{k=1}^{N}|\psi_k\rangle\langle\psi_k|\right)|\boldsymbol{\chi}\rangle = \langle\boldsymbol{\chi}|\boldsymbol{\psi}\rangle\langle\boldsymbol{\psi}|\boldsymbol{\chi}\rangle = \mathbf{C}\mathbf{C}^{\dagger} = \{\gamma_{u,w}\}. \tag{10.34}$$

It is proportional to the nonadditive component $T^{nadd.}[\boldsymbol{\chi}]$ of the system average kinetic energy: $T^{\mathrm{total}}[\boldsymbol{\chi}] = \mathrm{tr}(\boldsymbol{\gamma}\mathbf{T})$, where the kinetic-energy matrix in AO representation $\mathbf{T} = \{T_{k,l} = \langle\chi_k|\hat{\mathrm{T}}|\chi_l\rangle\}$.

In this general molecular scenario of the orbital approximation one uses the most extended (valence) basins of the negative CG density, $f^{nadd.}(\boldsymbol{r}) < 0$, enclosed by the corresponding $f^{nadd.}(\boldsymbol{r}) = 0$ surfaces, as locations of the system chemical bonds. This proposition has been recently validated numerically (Nalewajski et al. 2010a, b). These results have been obtained using the standard SCF MO calculations [GAMESS (1993) software] in the minimum AO basis; the STO-3G basis has been selected to facilitate a comparison with intuitive chemical considerations. In the remaining part of this section we present in Figs. 10.12–10.21 representative results of this extensive study (see also: Nalewajski 2010a, f). The contour maps, for the optimized geometries, will be reported in a.u. The negative CG basins, also shown in the perspective views, are identified by the broken-line contours. For the visualization purposes the Matpack and DISLIN graphic libraries have been used.

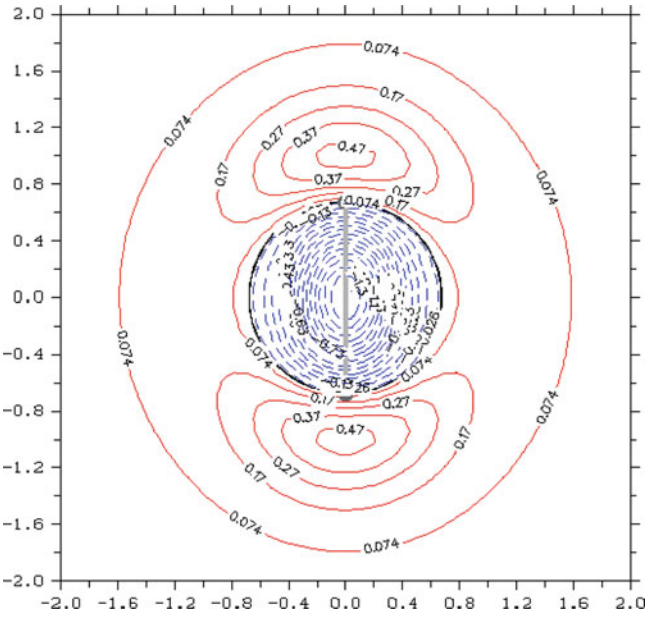

Fig. 10.12 The contour map of the CG density $f^{nadd.}(\boldsymbol{r})$ for H_2 (see also Fig. 10.10)

The contour map of Fig. 10.12 confirms qualitative predictions of Fig. 10.10. In this axial cut of $f^{nadd.}(\boldsymbol{r})$ for H_2 the nonadditive Fisher information is seen to be lowered in the spherical *bonding* region between the two nuclei. At the same time the accompanying increases in this quantity are observed in the nonbonding regions of each hydrogen atom, signifying the increased localization (structure) in this homonuclear diatomic due to the axial polarization of the initially spherical atomic densities. It should be stressed that the molecular CG integral over the whole space must be positive, since by the *virial theorem* for the equilibrium geometry the shift in kinetic component of the BO potential, relative to the separated atom (dissociation) limit, must be positive, thus giving rise to the overall *"production"* of the nonadditive Fisher information in the molecular hydrogen.

A similar analysis for HF is presented in Fig. 10.13. The perspective view of $f^{nadd.}(\boldsymbol{r}) < 0$ volumes (upper panel) and the contour map of the axial cut of $f^{nadd.}(\boldsymbol{r})$ (lower panel) indicate the existence of three basins of a decreased nonadditive Fisher information: a large, dominating (bonding) region Ω_1 located in the valence shells of two atoms, and the axially centered two small volumes detected in the inner-shell of fluorine. The shape of the bonding volume is seen to exhibit a polarization toward the $2p_\pi$ orbitals of a more electronegative fluorine atom.

In HCl (Fig. 10.14) one again observes two smaller (inner-shell) and a large (valence-shell) basins of the negative CG density. The softer heavy atom is now seen to undergo a more substantial inner-shell reconstruction in the nonadditive Fisher information. There is an axial build-up of $f^{nadd.}(\boldsymbol{r})$ seen in the nonbonding regions of two atoms, particularly on the hydrogen atom. It should be realized that

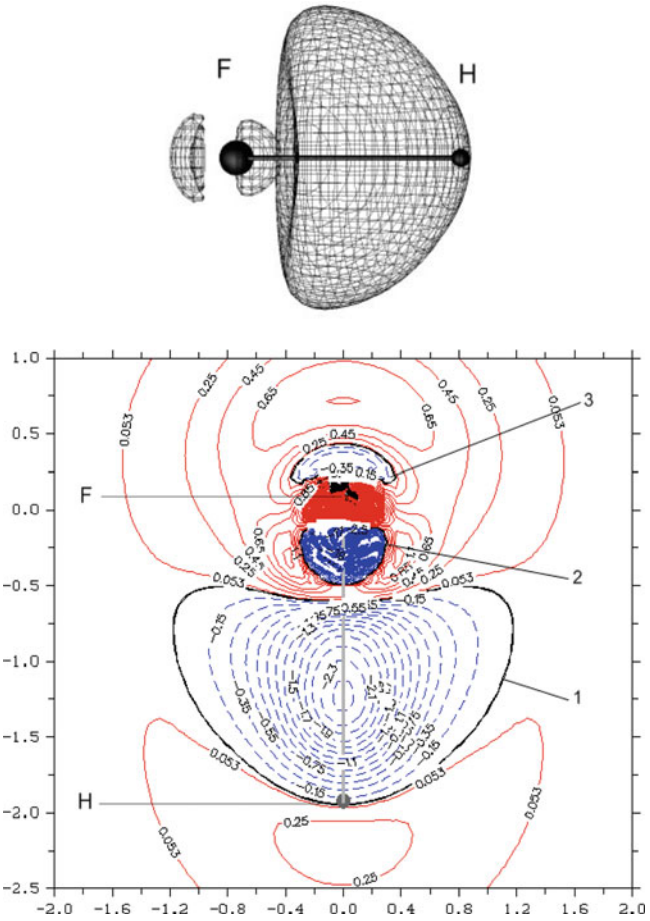

Fig. 10.13 The perspective view of the negative basins of CG (upper panel) and the contour map of the CG density (lower panel) for HF

compared to HF, where both atoms exhibit the "hard" (difficult to polarize) electron distributions in their valence shells, the (soft) chlorine atom combined with the (hard) hydrogen generates a stronger ionic (electron-transfer) component H → Cl, ultimately giving rise to the ionic pair H^+Cl^- in the dissociation limit, and hence a smaller covalent (electron-sharing) component H—Cl in the resultant chemical bond.

Consider next the triple chemical bond in N_2 (Fig. 10.15), where the bonding (valence) basin is now distinctly extended away from the bond axis, due to the presence of two π bonds accompanying the central σ bond. Small core-polarization basins, now symmetrically distributed near each constituent atom along the bond axis, are observed in the perspective view, while the *sp*-hybridization reconstruction of the nonbonding regions on both atoms is again much in evidence in the

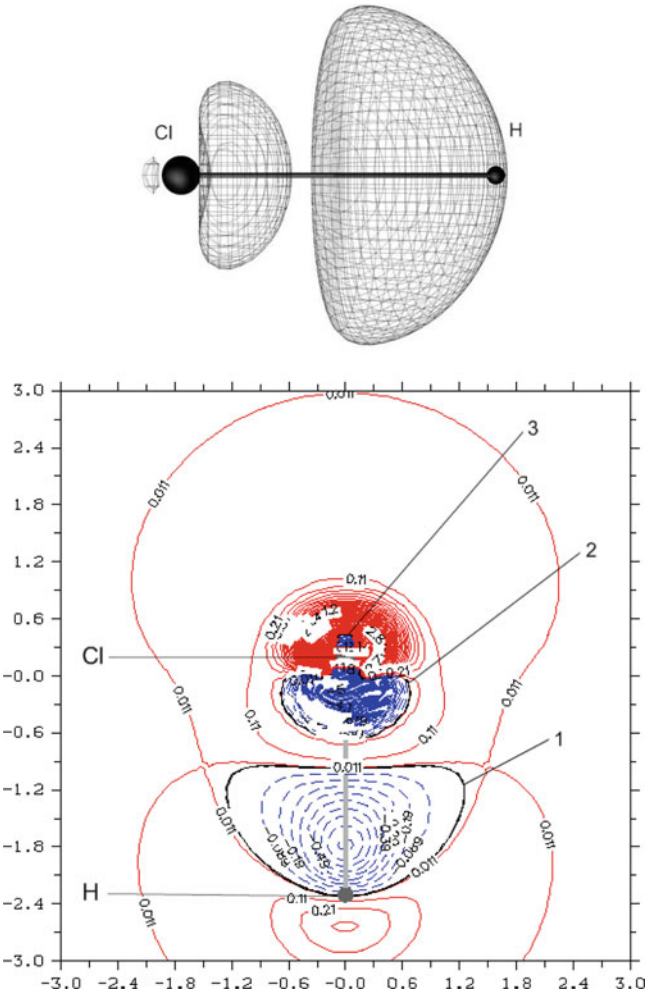

Fig. 10.14 The same as in Fig. 10.13 for HCl

accompanying contour map. The dominating (bonding) region around the bond middle-point is now "squeezed" between the two cores of nitrogen atoms. The small, axially placed core regions of the depleted contra-gradience are seen to be surrounded by the volumes of the positive values of this information density in transverse directions. They reflect the charge displacements accompanying the π-bond formation, which is also seen in the corresponding density difference diagram of Figs. 10.1 and 10.3.

In the water molecule (Fig. 10.16) one detects two slightly overlapping outer-basins of the negative nonadditive Fisher information in the O–H bonding regions, and two small inner-shell basins of the negative CG density on oxygen atom. The bonding basins, which define the two localized single bonds, are located between

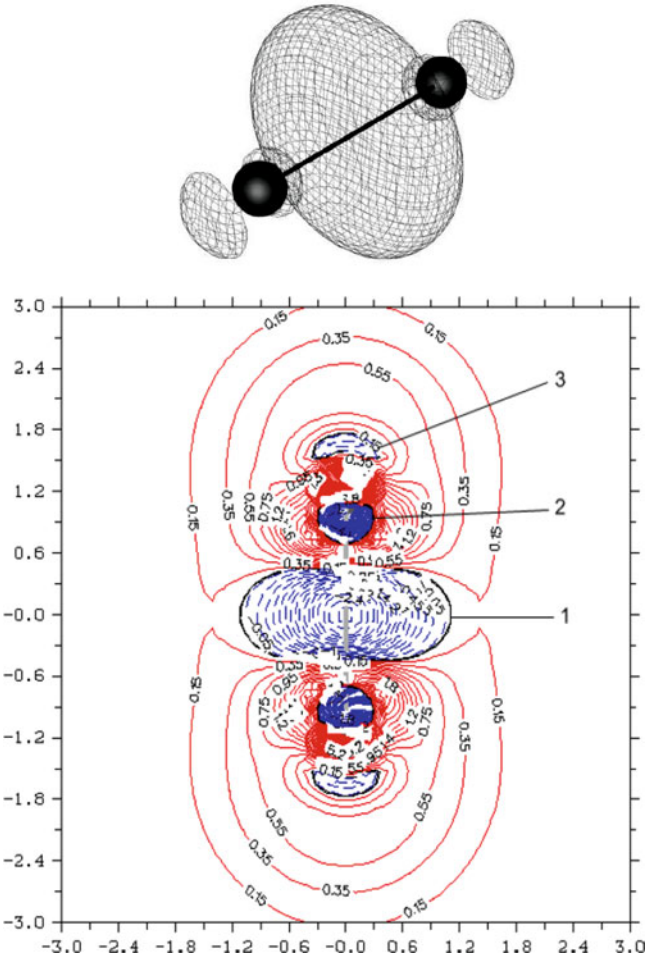

Fig. 10.15 The same as in Fig. 10.13 for N_2

the corresponding pairs of nuclei and the lowering of the CG density in each bond is seen to be the strongest in the direction linking the two O and H nuclear attractors. The overlapping character of these two regions of the negative nonadditive kinetic-energy, reflected by the present nonadditive Fisher-information probe, indicates a partial delocalization of the bonding electrons of one O–H bond into the bonding region of the other chemical bond, as indeed implied by the delocalized character of the occupied canonical MO. The contour map for the cut in the molecular plane also reveals a strong buildup of this information/kinetic-energy quantity in the lone-pair region of oxygen, and – to a lesser degree – in the nonbonding regions of two hydrogens. This effect on the heavy atom should indeed be expected as a result of its promotion due to the nearly tetrahedral sp^3-hybridization.

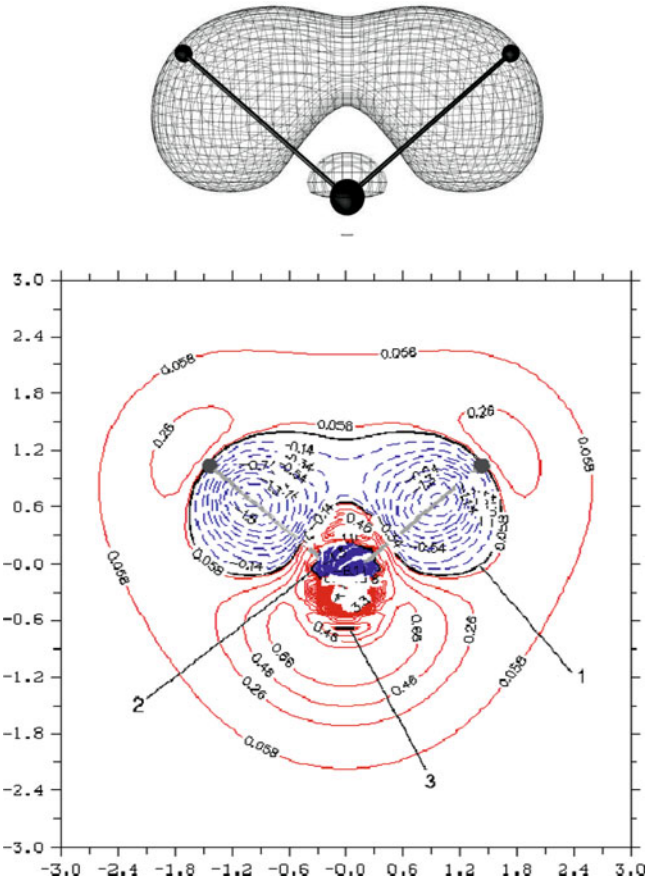

Fig. 10.16 The same as in Fig. 10.13 for H_2O

One thus concludes on the basis of this numerical evidence that CG criterion for detecting the valence basins of a diminished nonadditive Fisher information in AO-resolution indeed provides an efficient tool for locating the bonding regions in representative diatomics. It diagnoses all typical displacements of the bonded atoms in the bond formation process, relative to the corresponding free atoms of the promolecule, which have already been diagnosed from the density difference diagrams, e.g., the AIM polarization *via* the promotion/hybridization mechanism, the interatomic CT, and the constructive interference of AO in the bonding region, which is responsible for the electron accumulation between the covalently bonded atoms.

The chemical bonds in small hydrocarbons are investigated in contour maps of Figs. 10.17–10.20. These diagrams testify to the efficiency of the CG criterion in localizing all C–C and C–H bonding regions in ethane, ethylene, acetylene, butadiene, and benzene. The CG pattern of the triple bond between the carbon

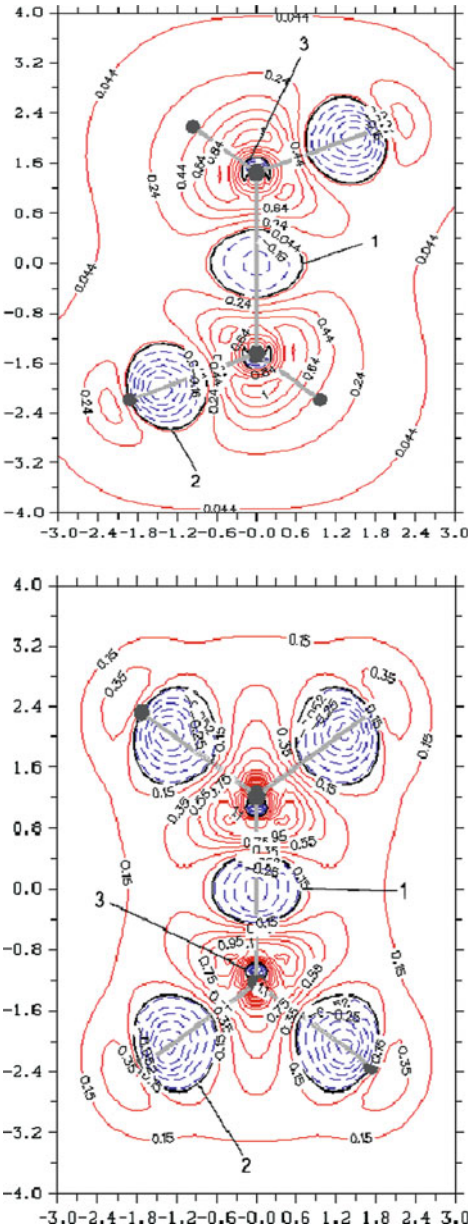

Fig. 10.17 The same as in Fig. 10.12 for ethane (upper panel) and ethylene (lower panel)

atoms in acetylene (upper panel of Fig. 10.18) strongly resembles that observed in N_2 (Fig. 10.15). In acetylene the two cylindrical bonding regions of the C–H bonds, axially extended due to a strong linear promotion of both carbon atoms *via* the *sp*-hybridization, and the central bonding basin due to the triple C–C bond, now transversely extended in the directions perpendicular to the bond axis, can be

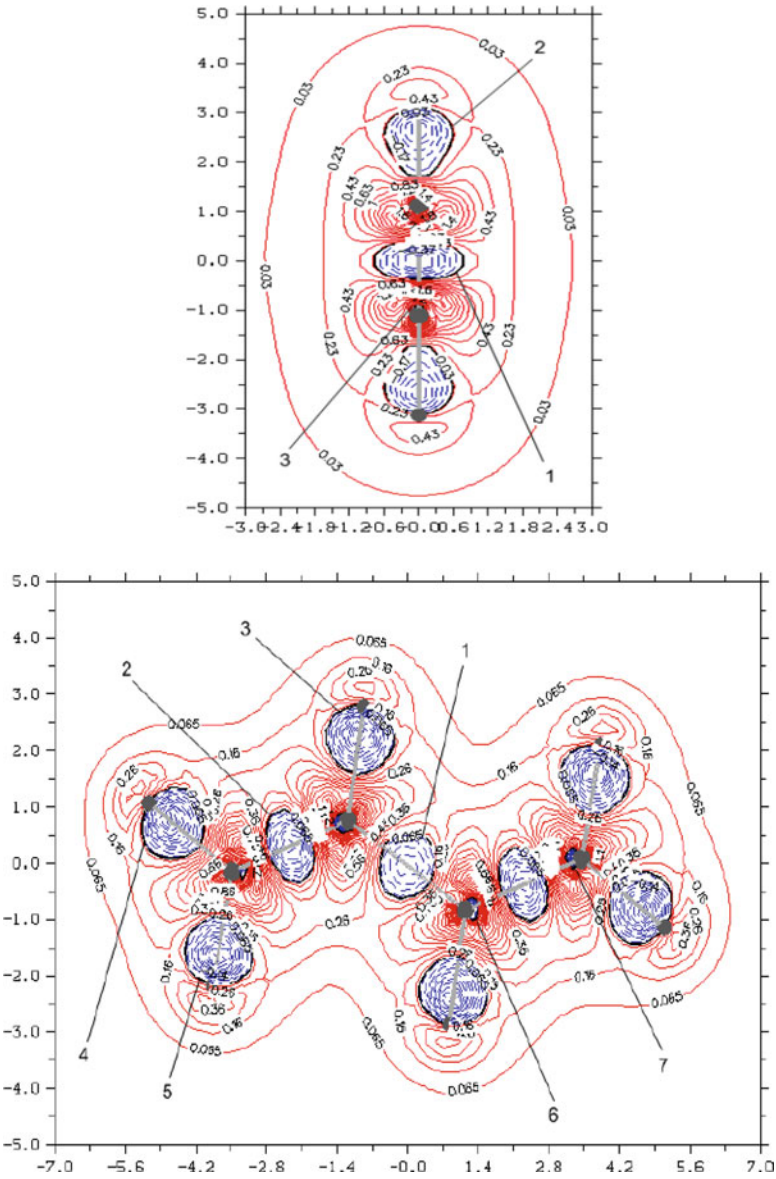

Fig. 10.18 The same as in Fig. 10.12 for acetylene (upper panel) and butadiene (lower panel)

clearly seen in the contour map. The $f^{nadd.}(\boldsymbol{r}) > 0$ regions on each carbon atom, very much resembling the atomic $2p_\pi$ distributions, reflect the presence of the bond π component. The depletion of the $2p_\pi$ electron density near the carbon nuclei generates more structure in the electron π-donating (nonbonding) regions of both

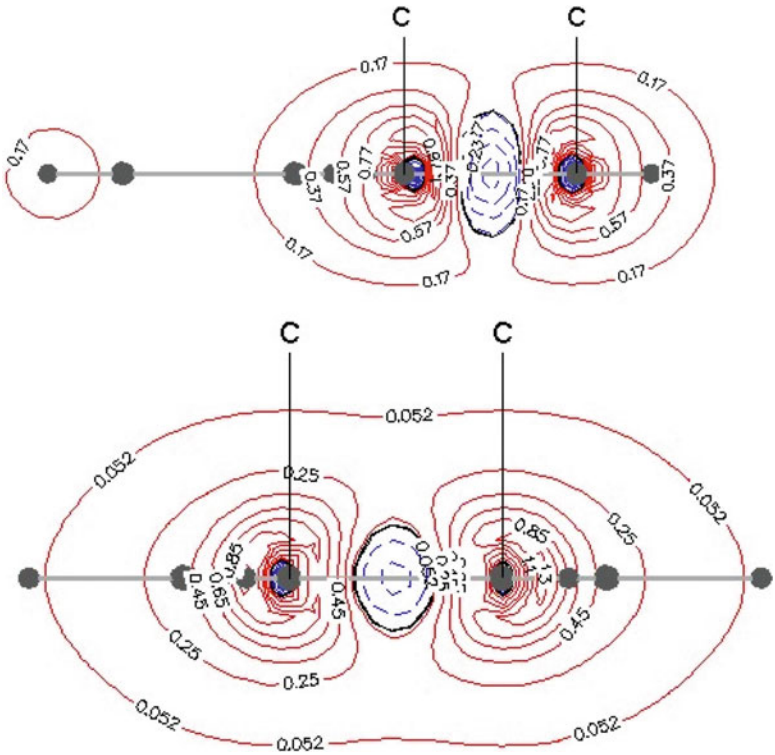

Fig. 10.19 The same as in Fig. 10.18 for the planes of section perpendicular to the molecular plane in butadiene passing through the peripheral (upper diagram) and middle (lower diagram) C—C bond axis

carbon atoms, and hence less structure (more delocalization) in the π-accepting (bonding) volume between the two nuclei.

The butadiene contour map in the molecular plane containing all nuclei is shown in the lower panel in Fig. 10.18. As seen in this diagram all bonds are properly accounted for by the IT CG probe. The same conclusion follows from examining Fig. 10.20, where the CG contour maps for benzene are shown, in the molecular plane (upper diagram) and in the perpendicular section containing the C–C bond (lower panel). It also follows from Fig. 10.19, where the additional CG cuts for butadiene are shown, in the planes of sections perpendicular to the molecular plane, along the peripheral and middle C–C bonds, respectively, that the π bond between the neighboring peripheral carbons in butadiene is indeed stronger than its central counterpart, in full accord with familiar quantum chemical predictions from the SCF LCAO MO theory.

Finally, the bonding patterns in a series of four small propellanes of Fig. 10.4 are examined in CG contour maps of Fig. 10.21. Each row of the figure is devoted to a different propellane, arranged from the smallest [1.1.1] molecule, exhibiting three single-carbon bridges, to the largest [2.2.2] system, consisting of three double-

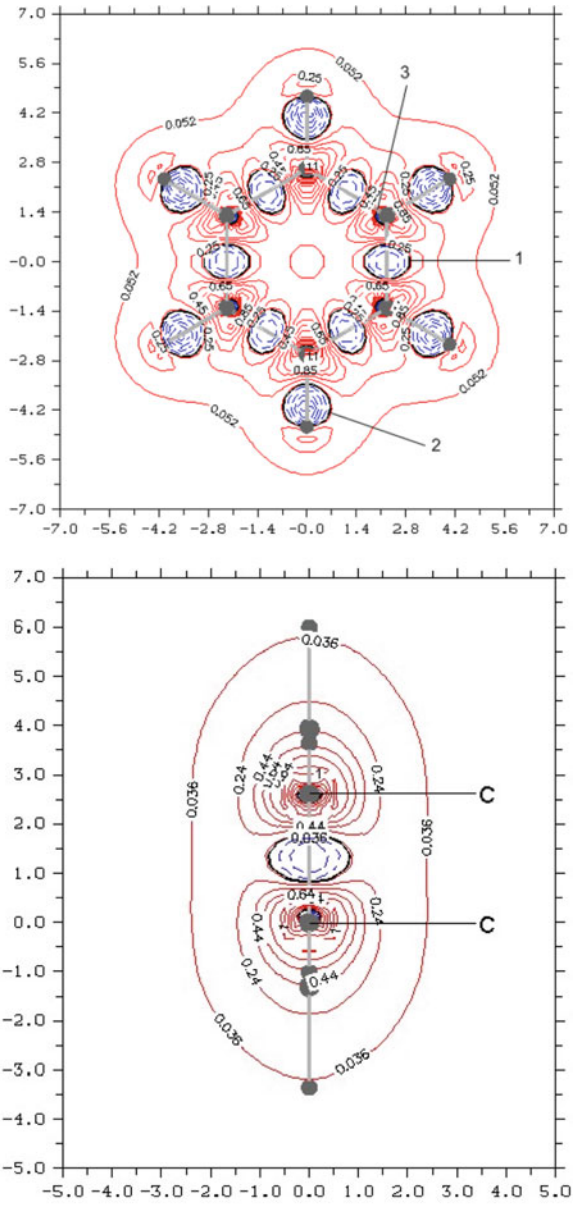

Fig. 10.20 The same as in Fig. 10.12 for benzene. The upper panel shows the contour map in the molecular plane, while the lower panel corresponds to the perpendicular plane of section passing through one of the C—C bonds

carbon bridges; the left panel of each row corresponds to the plane of section perpendicular to the central bond between the bridgehead carbons, at the bond midpoint, while the axial cut of the right panel involves one of the system carbon bridges.

The main result of the previous IT and density-difference analyses, the apparent lack of the *direct* (through-space) bond between the carbon bridgeheads in the

[1.1.1] and [2.1.1] systems, and a presence of practically single bond in the [2.2.1] and [2.2.2] propellanes, remain generally confirmed by the new CG probe, but this transition is now seen to be less sharp, with very small bonding basins between bridgeheads being also observed in the two smallest molecules. Thus, in accordance with the CG criterion the transition from the missing direct bonding in [1.1.1] system to the full, direct central bond in [2.2.2] propellane appears to be less abrupt: a very small bonding basin identified in the former case is steadily evolving into that attributed to the full bond in both [2.2.1] and [2.2.2] propellanes. The C–C and C–H chemical bonds in the bridges are again perfectly delineated by the valence surfaces of the vanishing CG density. The observed patterns of the nonadditive

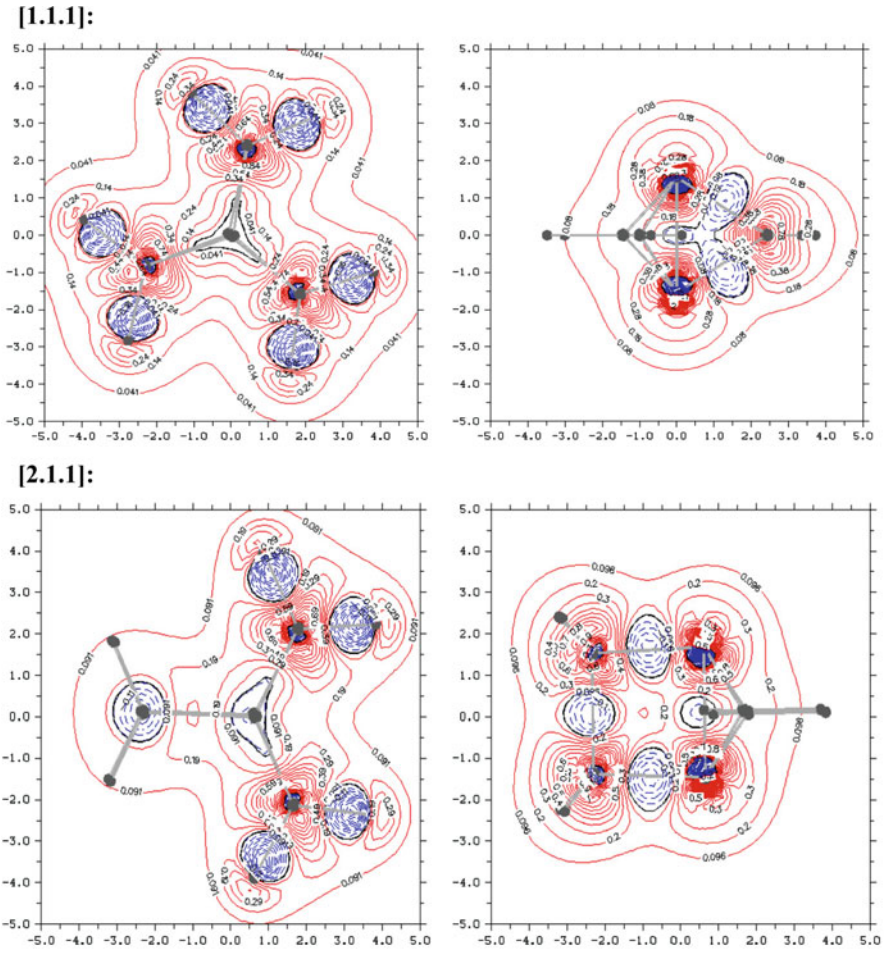

Fig. 10.21 (continued)

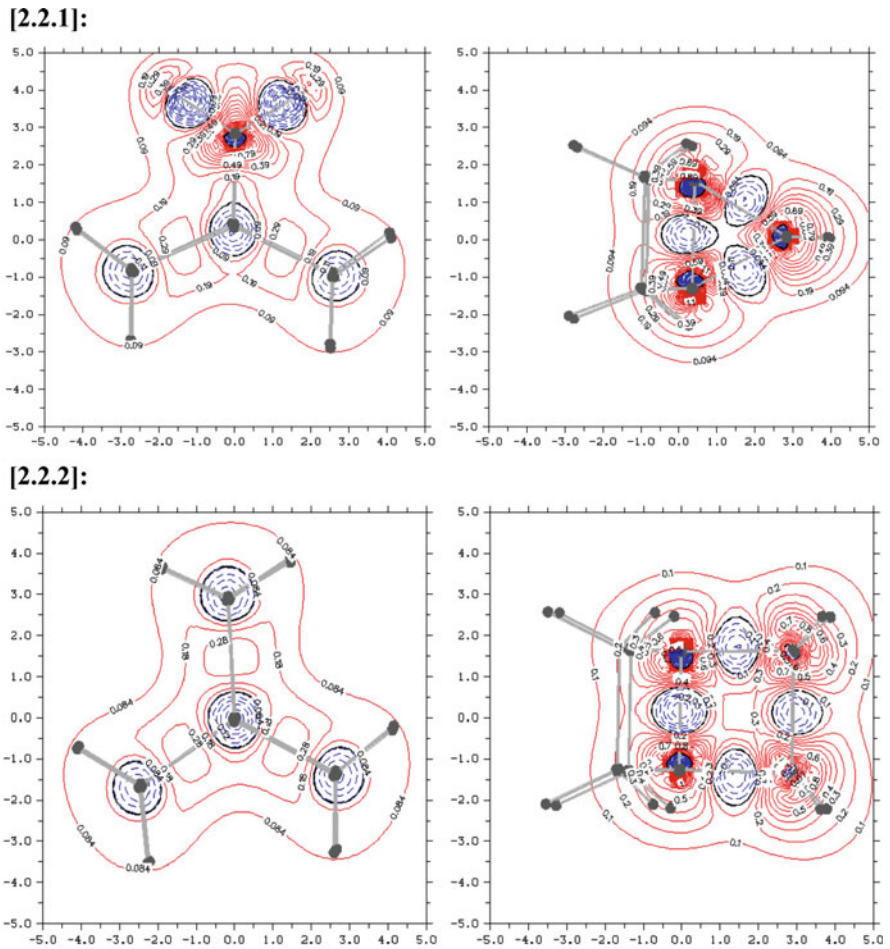

Fig. 10.21 The same as in Fig. 10.12 for the four propellanes of Fig. 10.4

Fisher information density always appear to be very much polarizational in character, with the closed bonding-regions of the negative CG being separated by the molecular environment of the positive values of this quantity, marking the system nonbonding regions.

References

Becke AD, Edgecombe KE (1990) J Chem Phys 92:5397
Casida ML, Wesołowski TA (2004) Int J Quantum Chem 96:577
Cortona P (1991) Phys Rev B 44:8454

Fuentalba P, Guerra D, Savin A (2009) In: Chattaraj PK (ed) Chemical reactivity theory: a density functional view. CRC, Boca Raton, p 281
Gopinathan MS, Jug K (1983) Theor Chim Acta (Berl.) 63:497, 511
Gordon RG, Kim YS (1972) J Chem Phys 56:3122
Hirshfeld FL (1977) Theor Chim Acta (Berl) 44:129
Jug K, Gopinathan MS (1990) In: Maksić ZB (ed) Theoretical models of chemical bonding, vol 2. Springer, Heidelberg, p 77
Mayer I (1983) Chem Phys Lett 97:270
Mayer I (1985) Theor Chim Acta (Berl.) 67:315
Mrozek J, Nalewajski RF, Michalak A (1998) Polish J Chem 72:1779
Nalewajski RF (2002a) Phys Chem Chem Phys 4:1710
Nalewajski RF (2002f) In: Barone V, Bencini A, Fantucci P (eds) Recent advances in density functional methods, part III. World Scientific, Singapore, p 257
Nalewajski RF (2003e) Mol Phys 101:2369
Nalewajski RF (2004b) Chem Phys Lett 386:265
Nalewajski RF (2006g) Information theory of molecular systems. Elsevier, Amsterdam
Nalewajski RF (2008e) Int J Quantum Chem 108:2230
Nalewajski RF (2009e) Int J Quantum Chem 109:425
Nalewajski RF (2009f) Int J Quantum Chem 109:2495
Nalewajski RF (2009g) Adv Quant Chem 56:217
Nalewajski RF (2010a) J Math Chem 47:667
Nalewajski RF (2010b) J Math Chem 47:692
Nalewajski RF (2010c) J Math Chem 47:709
Nalewajski RF (2010d) J Math Chem 47:808
Nalewajski RF (2010f) Information origins of the chemical bond. Nova Science, New York
Nalewajski RF (2010g) J Math Chem 48:752
Nalewajski RF (2011a) J Math Chem 49:371
Nalewajski RF (2011b) J Math Chem 49:546
Nalewajski RF (2011c) J Math Chem 49:806
Nalewajski RF (2011d) J Math Chem 49:592
Nalewajski RF (2011e) J Math Chem 49:2308
Nalewajski RF (2011f) Int J Quantum Chem (in press)
Nalewajski RF, Broniatowska E (2003a) J Phys Chem A 107:6270
Nalewajski RF, Gurdek P (2011a) J Math Chem 49:1226
Nalewajski RF, Gurdek P (2011b) Struct Chem (in press)
Nalewajski RF, Mrozek J (1994) Int J Quantum Chem 51:187
Nalewajski RF, Mrozek J (1996) Int J Quantum Chem 57:377
Nalewajski RF, Parr RG (2000) Proc Natl Acad Sci USA 97:8879
Nalewajski RF, Parr RG (2001) J Phys Chem A 105:7391
Nalewajski RF, Świtka E (2002) Phys Chem Chem Phys 4:4952
Nalewajski RF, Köster AM, Jug K (1993) Theor Chim Acta (Berl.) 85:463
Nalewajski RF, Formosinho SJ, Varandas AJC, Mrozek J (1994a) Int J Quantum Chem 52:1153
Nalewajski RF, Mrozek J, Mazur G (1996b) Can J Chem 100:1121
Nalewajski RF, Mrozek J, Michalak A (1997) Int J Quantum Chem 61:589
Nalewajski RF, Świtka E, Michalak A (2002) Int J Quantum Chem 87:198
Nalewajski RF, Köster AM, Escalante S (2005) J Phys Chem A 109:10038
Nalewajski RF, de Silva P, Mrozek J (2010a) Kinetic-energy/Fisher-information indicators of chemical bonds. In: Wang A, Wesołowski TA (eds) Kinetic energy functional. World Scientific, Singapore (in press)
Nalewajski RF, de Silva P, Mrozek J (2010b) J Mol Struct THEOCHEM 954:57
Savin A, Nesper R, Wengert S, Fässler TF (1997) Angew Chem Int Ed Engl 36:1808
Silvi B, Savin A (1994) Nature 371:683

Wesołowski TA (2004a) J Am Chem Soc 126:11444
Wesołowski TA (2004b) Chimia 58:311
Wesołowski TA, Tran F (2003) J Chem Phys 118:2072
Wesołowski TA, Warshel A (1993) J Phys Chem 97:8050
Wesołowski TA, Weber J (1998) Chem Phys Lett 248:71
Wesołowski TA, Muller RP, Warshel A (1995) J Phys Chem 100:15444
Wiberg KB (1968) Tetrahedron 24:1083